*Planck 2013 results*

# *Planck* 2013 results. X. HFI energetic particle effects: characterization, removal, and simulation

Planck Collaboration: P. A. R. Ade[83], N. Aghanim[58], C. Armitage-Caplan[87], M. Arnaud[70], M. Ashdown[67,6], F. Atrio-Barandela[18], J. Aumont[58], C. Baccigalupi[82], A. J. Banday[90,10], R. B. Barreiro[64], E. Battaner[91], K. Benabed[59,89], A. Benoît[56], A. Benoit-Lévy[25,59,89], J.-P. Bernard[90,10], M. Bersanelli[35,49], P. Bielewicz[90,10,82], J. Bobin[70], J. J. Bock[65,11], J. R. Bond[9], J. Borrill[14,84], F. R. Bouchet[59,89], M. Bridges[67,6,62], M. Bucher[1], C. Burigana[48,33], J.-F. Cardoso[71,1,59], A. Catalano[72,69], A. Challinor[62,67,12], A. Chamballu[70,15,58], H. C. Chiang[28,7], L.-Y Chiang[61], P. R. Christensen[78,38], S. Church[86], D. L. Clements[54], S. Colombi[59,89], L. P. L. Colombo[24,65], F. Couchot[68], A. Coulais[69], B. P. Crill[65,79], A. Curto[6,64], F. Cuttaia[48], L. Danese[82], R. D. Davies[66], P. de Bernardis[34], A. de Rosa[48], G. de Zotti[44,82], J. Delabrouille[1], J.-M. Delouis[59,89], F.-X. Désert[52], J. M. Diego[64], H. Dole[58,57], S. Donzelli[49], O. Doré[65,11], M. Douspis[58], X. Dupac[40], G. Efstathiou[62], T. A. Enßlin[75], H. K. Eriksen[63], F. Finelli[48,50], O. Forni[90,10], M. Frailis[46], E. Franceschi[48], S. Galeotta[46], K. Ganga[1], M. Giard[90,10], D. Girard[72], Y. Giraud-Héraud[1], J. González-Nuevo[64,82], K. M. Górski[65,92], S. Gratton[67,62], A. Gregorio[36,46], A. Gruppuso[48], F. K. Hansen[63], D. Hanson[76,65,9], D. Harrison[62,67], S. Henrot-Versillé[68], C. Hernández-Monteagudo[13,75], D. Herranz[64], S. R. Hildebrandt[11], E. Hivon[59,89], M. Hobson[6], W. A. Holmes[65], A. Hornstrup[16], W. Hovest[75], K. M. Huffenberger[26], A. H. Jaffe[54], T. R. Jaffe[90,10], W. C. Jones[28], M. Juvela[27], E. Keihänen[27], R. Keskitalo[22,14], T. S. Kisner[74], R. Kneissl[39,8], J. Knoche[75], L. Knox[29], M. Kunz[17,58,3], H. Kurki-Suonio[27,42], G. Lagache[58], J.-M. Lamarre[69], A. Lasenby[6,67], R. J. Laureijs[41], C. R. Lawrence[65], R. Leonardi[40], C. Leroy[58,90,10], J. Lesgourgues[88,81], M. Liguori[32], P. B. Lilje[63], M. Linden-Vørnle[16], M. López-Caniego[64], P. M. Lubin[30], J. F. Macías-Pérez[72], N. Mandolesi[48,5,33], M. Maris[46], D. J. Marshall[70], P. G. Martin[9], E. Martínez-González[64], S. Masi[34], M. Massardi[47], S. Matarrese[32], F. Matthai[75], P. Mazzotta[37], P. McGehee[55], A. Melchiorri[34,51], L. Mendes[40], A. Mennella[35,49], M. Migliaccio[62,67], A. Miniussi[58], S. Mitra[53,65], M.-A. Miville-Deschênes[58,9], A. Moneti[59], L. Montier[90,10], G. Morgante[48], D. Mortlock[54], S. Mottet[59], D. Munshi[83], J. A. Murphy[77], P. Naselsky[78,38], F. Nati[34], P. Natoli[33,4,48], C. B. Netterfield[20], H. U. Nørgaard-Nielsen[16], F. Noviello[66], D. Novikov[54], I. Novikov[78], S. Osborne[86], C. A. Oxborrow[16], F. Paci[82], L. Pagano[34,51], F. Pajot[58], D. Paoletti[48,50], F. Pasian[46], G. Patanchon[1,⋆], O. Perdereau[68], L. Perotto[72], F. Perrotta[82], F. Piacentini[34], M. Piat[1], E. Pierpaoli[24], D. Pietrobon[65], S. Plaszczynski[68], E. Pointecouteau[90,10], G. Polenta[4,45], N. Ponthieu[58,52], L. Popa[60], T. Poutanen[42,27,2], G. W. Pratt[70], G. Prézeau[11,65], S. Prunet[59,89], J.-L. Puget[58], J. P. Rachen[21,75], B. Racine[1], M. Reinecke[75], M. Remazeilles[66,58,1], C. Renault[72], S. Ricciardi[48], T. Riller[75], I. Ristorcelli[90,10], G. Rocha[65,11], C. Rosset[1], G. Roudier[1,69,65], B. Rusholme[55], L. Sanselme[72], D. Santos[72], A. Sauvé[90,10], G. Savini[80], D. Scott[23], E. P. S. Shellard[12], L. D. Spencer[83], J.-L. Starck[70], V. Stolyarov[6,67,85], R. Stompor[1], R. Sudiwala[83], F. Sureau[70], D. Sutton[62,67], A.-S. Suur-Uski[27,42], J.-F. Sygnet[59], J. A. Tauber[41], D. Tavagnacco[46,36], L. Terenzi[48], L. Toffolatti[19,64], M. Tomasi[49], M. Tristram[68], M. Tucci[17,68], G. Umana[43], L. Valenziano[48], J. Valiviita[42,27,63], B. Van Tent[73], P. Vielva[64], F. Villa[48], N. Vittorio[37], L. A. Wade[65], B. D. Wandelt[59,89,31], D. Yvon[15], A. Zacchei[46], and A. Zonca[30]

*(Affiliations can be found after the references)*

**ABSTRACT**

We describe the detection, interpretation, and removal of the signal resulting from interactions of high energy particles with the *Planck* High Frequency Instrument (HFI). There are two types of interactions: heating of the 0.1 K bolometer plate; and glitches in each detector time stream. The transient responses to detector glitch shapes are not simple single-pole exponential decays and fall into three families. The glitch shape for each family has been characterized empirically in flight data and these shapes have been used to remove glitches from the detector time streams. The spectrum of the count rate per unit energy is computed for each family and a correspondence is made to the location on the detector of the particle hit. Most of the detected glitches are from Galactic protons incident on the die frame supporting the micro-machined bolometric detectors. In the *Planck* orbit at L2, the particle flux is around $5 \, \mathrm{cm}^{-2} \, \mathrm{s}^{-1}$ and is dominated by protons incident on the spacecraft with energy >39 MeV, at a rate of typically one event per second per detector. Different categories of glitches have different signatures in the time stream. Two of the glitch types have a low amplitude component that decays over nearly 1 s. This component produces excess noise if not properly removed from the time-ordered data. We have used a glitch detection and subtraction method based on the joint fit of population templates. The application of this novel glitch subtraction method removes excess noise from the time streams. Using realistic simulations, we find that this method does not introduce signal bias into the *Planck* data.

**Key words.** cosmic background radiation – cosmology: observations – instrumentation: detectors – space vehicles: instruments – methods: data analysis

---

⋆ Corresponding author: G. Patanchon, e-mail: `patanchon@apc.univ-paris-Diderot.fr`

# 1. Introduction

This paper, one of a set associated with the 2013 release of data from the *Planck*[1] mission (Planck Collaboration I 2014), describes the detection of high energy particle impacts on the 0.1 K stage and bolometric detectors in the *Planck* High Frequency Instrument (HFI, Lamarre et al. 2010) and removal of these systematic effects from the millimetre and submillimetre signals. A full description of the HFI can be found elsewhere (Planck HFI Core Team 2011a,b; Planck Collaboration VI 2014; Planck Collaboration VII 2014; Planck Collaboration VIII 2014; Planck Collaboration IX 2014).

Bolometers (Holmes et al. 2008), such as those used in HFI on *Planck*, are phonon-mediated thermal detectors with finite response time to changes in the absorbed optical power. The bolometer consists of a micro-machined silicon nitride (Si-N) mesh absorber with a germanium (Ge) thermistor suspended from the Si die frame. Each bolometer is mounted on a metal housing, and these are assembled into two types of bolometer modules, as shown in Fig. 1: a spider web bolometer (SWB, Bock et al. 1995) which detects total power; and a polarization sensitive bolometer (PSB, Jones et al. 2007). In the PSB module there are two bolometers to independently measure power in each of the two linear polarizations. The bolometers are mounted on a copper-plated stainless steel plate cooled to 0.1 K and stabilized within a few microkelvin of the temperature set point. Two "dark" bolometer modules are blanked off at the 0.1 K plate and are used to monitor systematic effects. The 0.1 K bolometer plate is surrounded by a roughly 1.5 mm thick aluminium box cooled to 4.5 K. Light is coupled into each bolometer module using a feedhorn at 4.5 K and a filter stack at 1.5 K (Lamarre et al. 2010).

At the Earth-Sun Lagrange point L2, high energy particles from the Sun and Galactic sources – primarily protons, electrons and helium nuclei – are incident on the spacecraft. This particle flux causes two main effects in HFI that have been reported previously. There is a time-variable thermal load on the 0.1 K plate (Planck Collaboration II 2011) and a significant rate of glitches in the bolometric signal (Planck HFI Core Team 2011b). In this paper, we report on the evolution of these effects over the entire period of HFI operations, from 3 July 2009 to 14 January 2012, and describe the analysis technique used to remove the effect of glitches from the data. Three families of glitches, "long", "short", and "slow" (or "longer" as named in Planck HFI Core Team 2011b), were found by comparing and stacking many events. Their characteristics are detailed in Sect. 2. Long glitches dominate the overall counts and exhibit an additional slow decay with a time constant of the order of 2 s, requiring template subtraction from the data. The new analysis, presented in Sect. 3.1, employs a joint fitting of the three glitch family templates and removal of the slow tails. In Sects. 3.2 and 4 we show that our adopted technique improves the noise performance of HFI. We have simulated the effect of the glitches on the data quality and find that systematic biases are small, contributing $<10^{-4}$ to the cosmological power spectrum.

We also present the coincident counts, energy distribution, total counts, and variations of glitch shapes within each family. These data, taken together with the beam-line and laboratory
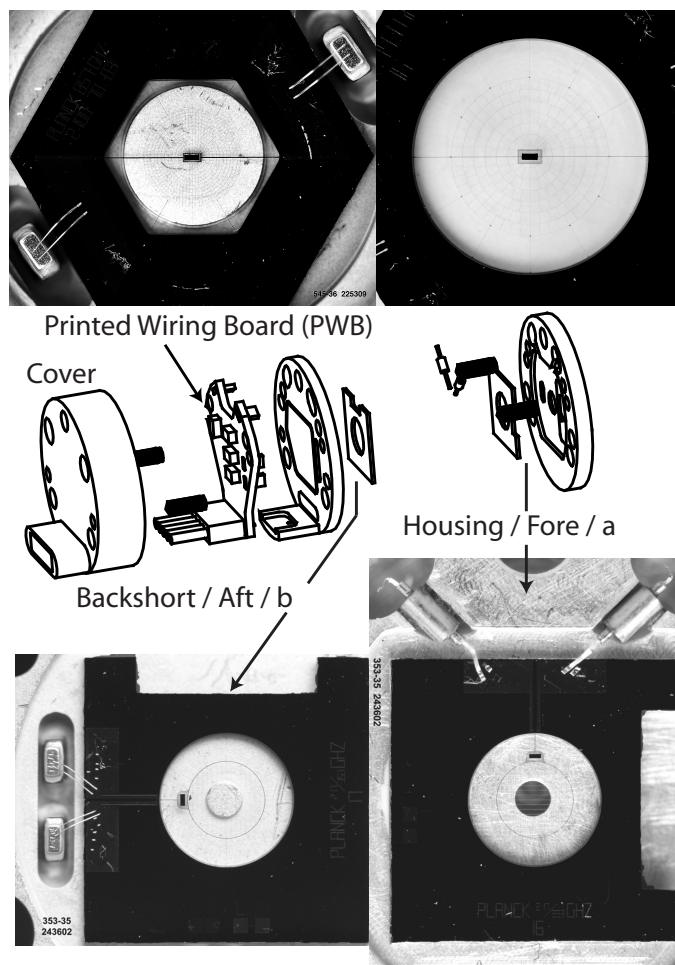
**Fig. 1.** *Top left and right*: completed multimode (see Maffei et al. 2010) 545 GHz and single-mode 143 GHz SWB bolometer modules. *Middle*: an exploded view of the assembly of a PSB (showing the definition of the "a" and "b" detectors of the pair). Alignment pins, shown in solid black, fix the aft and fore bolometer assemblies to an angular precision of $<0.1°$. The SWB assembly is similar to the PSB aft bolometer assembly and does not include a feedhorn aperture integrated with the module package. *Bottom*: PSB pair epoxied in the module parts prior to mating. To the *right*, the feedhorn aperture can be seen through the fore bolometer in the housing. To the *left*, the quarter-wave backshort can be seen through the aft bolometer absorber mesh.

tests using spare HFI bolometers (Catalano et al. 2014; Planck Collaboration II 2011), allow identification of the physical cause of the glitch events for two of the types (Sect. 5). Long glitches are due to energy absorption events in the Si die and short glitches are due to events in the optical absorbing grid or Ge thermistor. The cause of the slow glitches, however, has not been identified. We also describe some rare effects not previously reported, including the response of the instrument to solar flares, secondary showers, and large high-energy events.

# 2. Glitch families

For instruments with bolometric detectors fielded on balloons (Crill et al. 2003; Masi et al. 2006; Benoît et al. 2003; Patanchon et al. 2008) and space missions (see Griffin et al. 2010, for *Herschel*-SPIRE), the glitches are flagged in the data time stream and then the flagged data are omitted. For most of these instruments, the transfer function is deconvolved from the time stream prior to flagging glitches. This has the benefit of increasing
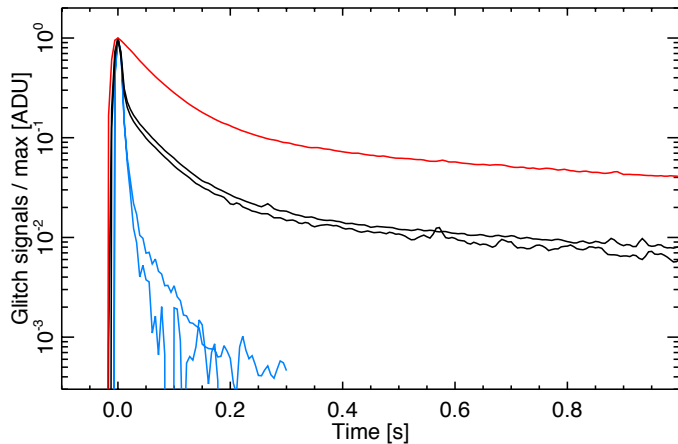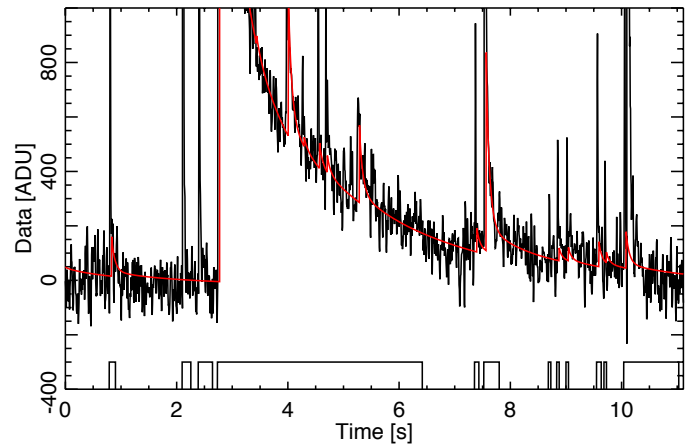
**Fig. 2.** Examples of three distinct families of glitch transfer functions for a typical PSB-a bolometer. Events like the blue curves are called "short" events, those like the black curves are called "long", and those like the red curves are called "slow". Typical variation of the shape within each family is shown for short and long glitches. The differences between long glitch shapes are modelled by a single nonlinearity parameter relating the amplitude of the slow tail of events with their peak amplitude. There is no apparent glitch tail associated with short events.



**Fig. 3.** Black: segment of raw data for one detector at 143 GHz before any deglitching; an estimate of the sky signal has been subtracted. Red: a time stream reconstructed from the estimated templates of long glitches with the method presented in Sect. 3.1. We have chosen a region in the vicinity of a large event. Data that are flagged for the analysis are indicated by the lines at the bottom of the figure. Notice the high level of confusion between long glitch signals.

the signal-to-noise ratio on each glitch, which minimizes the fraction of falsely flagged data.

The population of glitches in *Planck* HFI is unusual. The glitch rate of ~1 s$^{-1}$ per detector is significantly higher than in the other instruments. Also, three distinct families of glitch transfer functions, shown in Fig. 2, are present in the data. The transfer function of each glitch family is described by a sum of three or four decaying exponential terms. For a given bolometer, the families, called short, long, and slow, are differentiated by the relative amplitudes of each term. Only the short glitches have a transfer function matching the instrument transfer function. The long glitches dominate the total rate and have a significant amplitude above the noise level, with a time constant >1 s as illustrated in Fig. 2. Deconvolving the instrument transfer function prior to glitch flagging did not improve glitch detection, and the large amplitude at times >1 s, which is the typical time between glitches, means there is glitch pile up. The high rate of long glitches leads to considerable confusion of glitch signals, as can be seen in Fig. 3, and makes it difficult to clean glitches in *Planck*-HFI data.

Omitting flagged data would lead to omission of >90% of the data, so we have developed a strategy to fit and to remove precise templates of long glitches from the time-ordered data. We take advantage of the excellent pointing accuracy (Planck Collaboration I 2011) and redundancy of the scan strategy, and have adopted a method that iterates between estimates of the signal from the sky and signal from the glitches (Planck HFI Core Team 2011b). A key to the effectiveness of this method, presented in Sect. 3.1, is a comprehensive understanding of the three families of glitches and a determination of the stability of these families over the course of the mission. In this section, we describe the features of the different glitch families that are relevant for their removal. Identification and classification of the glitches has been done using previous versions of the method, as introduced in Planck Collaboration VII (2014). This was an iterative process, since accurate glitch property determination is necessary to "tune" the method for effective detection and cleaning, and an efficient method is necessary to separate glitches into families and derive properties. Templates of each of the

three glitch families are obtained from stacking many normalized glitches, and the general features are derived from fitting the normalized decay profile with a sum of exponentials. The methodology is detailed in Sect. 3.1.4.

### 2.1. Short glitches

The highest-amplitude events are the short glitches. The short glitch time response, or template, is shown in Fig. 4. Short events have a rise time much shorter than the sampling period of 5 ms, followed by a fast decay. These rapid variations can cause oscillations in the electronics, and the response amplitude depends on the precise moment of the glitch within the sampling period. So throughout the paper, the amplitude of the glitch is defined as the peak value of the sampled data. The shortest exponential decay component has a time constant similar to the fast part of the optical transfer function; three additional terms (corresponding to the tail) have very low amplitudes ($<10^{-2}$ of the peak), and time constants of typically 40 ms, 400 ms, and 2 s. The 2 s decaying signal has an amplitude about $5 \times 10^{-5}$ of the peak and was detected only after stacking short glitches measured over the entire mission. The transfer function of short glitches nearly matches the instrument optical transfer function.

The time constants and amplitudes derived by fitting three exponentials to short glitch measurements are given in Fig. 5 for all the bolometers. The fit has been performed after stacking events with amplitudes between 1200 and 2400 times the noise (around 2 keV of deposited energy), which corresponds to energies of the transition between the two subcategories of short events. The 2 s time constant is not included in the template fit. We have verified that, given the counts of short glitches, and assuming a random distribution of glitches, the 2 s tails produce a signal that is three orders of magnitude lower than the white noise, and so can be neglected in the data processing. We observe some scatter of the values across bolometers, although this may reflect the degeneracies in the fit of the different time constants and amplitudes rather than variations of the template shape between bolometers. A careful study of the degeneracies
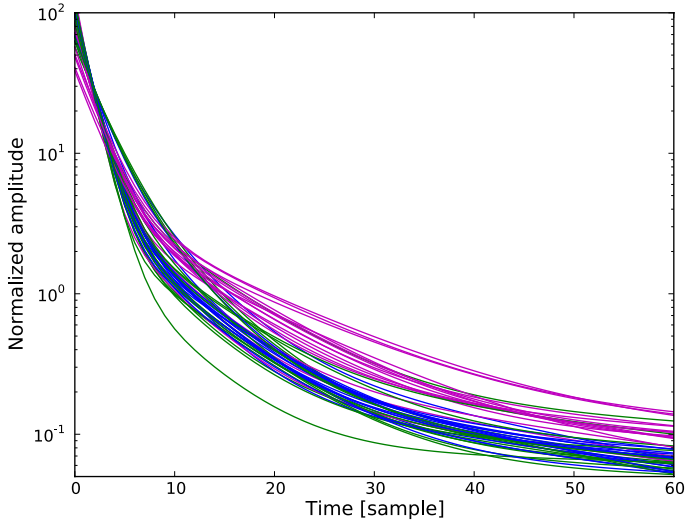
**Fig. 4.** Short glitch templates for all detectors obtained using the method discussed in Sect. 3.1.4. Blue lines are for PSB-a, green for PSB-b, and magenta for SWB (see Fig. 2 for the definition of the "a" and "b" bolometers in a PSB pair). One sample corresponds to 5 ms.



**Fig. 5.** Parameters of the glitch templates built from the sum of four decaying exponentials for long glitches and three exponentials for short glitches. Fitted amplitudes versus time constants for all exponentials are displayed for all bolometers. Stars indicate short glitches and circles indicate long glitches. The type of bolometer is indicated by colour (blue is PSB-a, green is PSB-b, and magenta is SWB). Values plotted are obtained after fitting exponentials on templates estimated by stacking a large number of events and normalized to one at the peak. A three-point filter was applied to the data prior to the fit of the exponentials (see text).

in the parameter fitting is presented in the analysis of the transfer function (Planck Collaboration VII 2014).
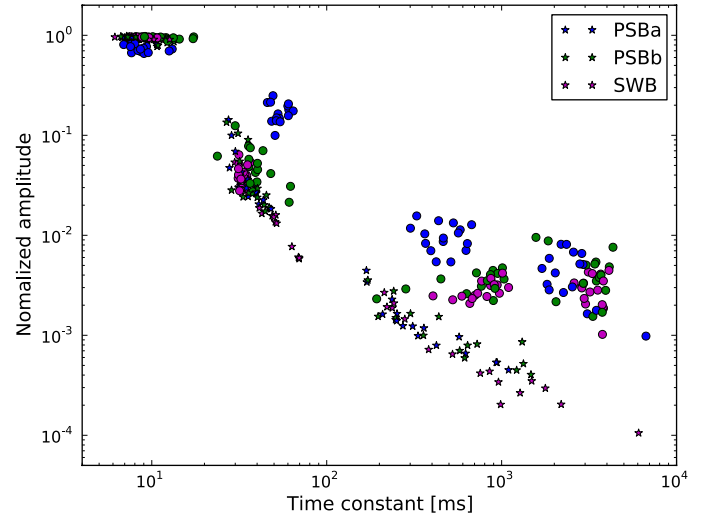
The amplitude of the tail is variable from event to event, but is small enough that its variability does not affect the processing of data. Moreover, we have found the existence of two subcategories of short glitches (one event of each subcategory is shown in Fig. 2), which can be distinguished by the amplitude of the tails. In fact, the tail has smaller amplitude for higher energy events and larger amplitude for lower energy events, with a variation of a factor of about two.
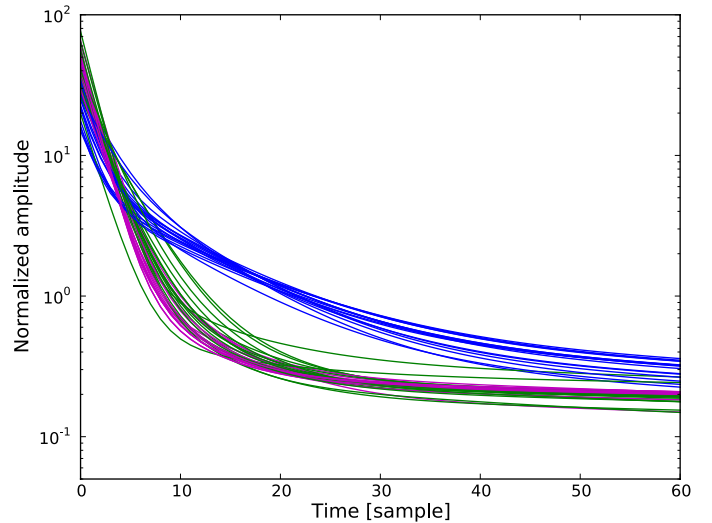
### 2.2. Long glitches

The long glitches are, on average, of lower amplitude than short glitches, but their rate is more than an order of magnitude greater. Most of the glitches in the HFI data are these long events. Their intermediate and slow decays are responsible for a noise excess at frequencies between 0.001 and 1 Hz (see Fig. 12), and they must be subtracted in order to reach the expected noise level. The rise time is very fast, much less than the sampling period, like the short glitches. The shortest exponential decay has a time constant similar to the fast part of the optical transfer function, followed by a tail with a much larger amplitude than we see for the short glitches. In Fig. 6 long glitch templates are shown for several bolometers. As with the short glitches, they are estimated by stacking a large number of events, and fitted with a sum of four exponential terms.

The slow tail has typical time constants of 50 ms, 500 ms, and 2 s for PSB-a bolometers and 35 ms, 500 ms and 2 s for PSB-b and SWB bolometers. The component with intermediate time constant (35 to 50 ms) starts with an amplitude relative to the peak of around 6% for PSB-a and around 3% for PSB-b and SWB bolometers. The components with long time constants (500 ms and 2 s) have an amplitude that is about 0.2% of the event peak.

The most striking feature in Fig. 6 is that the component with intermediate time constant decays faster and has lower amplitude for PSB-b and SWB than for PSB-a. The component with the longest time constant, ~2 s, has a similar amplitude for all



**Fig. 6.** Long glitch templates for all detectors. Blue is for PSB-a, green for PSB-b and magenta for SWB.

bolometers. The time constants and amplitudes are shown in Fig. 5 for all the bolometers.

We do not observe significant changes in the time constants of the long glitch tail from event to event. However, the amplitude of the long tail relative to the fast part does show significant dispersion (see Sect. 5.4). The quoted amplitudes of the long and intermediate tails are for lower energy events, but we find that the amplitude of the tail of long glitches (relative to the peak) is a function of the peak amplitude of the events. This nonlinearity can be described empirically to good accuracy with a simple linear function that is fitted and accounted for in the processing. The nonlinearity corresponds to a factor of two at most between the lowest and highest energies of detected events. This factor is lower for PSB-b and SWB bolometers. This is illustrated by
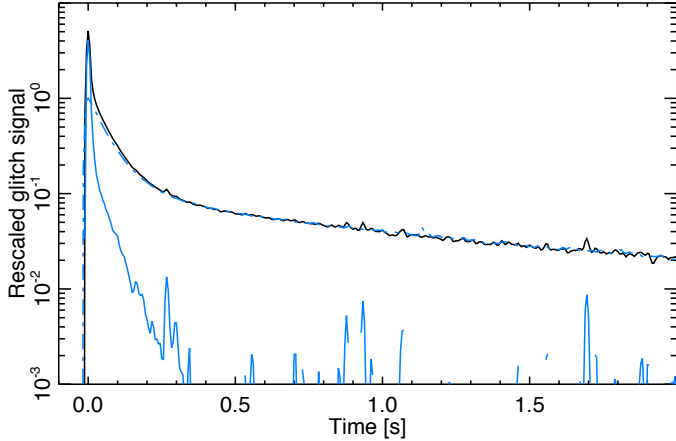
**Fig. 7.** Comparison of a long glitch (black) and a slow glitch (dot-dashed blue). For this plot, the two high energy events were rescaled to match after 200 ms. The difference is shown in blue.

Fig. 2, which shows two typical long events at different amplitudes, both normalized to the peak. The difference in amplitude of the slow tail is clearly visible.

Finally, in a small proportion of events the ratio of amplitude of the fast part to that of the slow part is different from the majority of long glitches. In particular, slightly less than 10% of events have a smaller amplitude tail than long glitches and about 0.5% have a higher tail (not including slow glitches). Those events do not fit into any of the categories of glitches, but their slow decaying tails, after $\approx$20 ms from the peak amplitude, are similar to the long glitches. Because of this, they are implicitly accounted for in the glitch removal procedure.

### 2.3. Slow glitches

Slow glitches are detected only for PSB-a. They have a rise time comparable to the optical time constant, i.e., much slower than the two other glitch families. The tail of a slow glitch is similar to that of a long glitch. Figure 7 shows a comparison of a high amplitude long glitch event with a slow glitch. The intermediate time constant of long glitches, which is of the order of 50 ms for PSB-a, is slightly (but significantly) larger for slow glitches, and this time constant is the fastest for those events, as can be seen in Fig. 7. The two tails are proportional to good accuracy from about 200 ms after the peak amplitude. Even with these differences, the long glitch template for a given bolometer is a good proxy for the slow glitches in the same bolometer.

### 2.4. Population counts

Figure 8 shows the distribution d$N$/d$E$ of the three populations of glitches for one detector as a function of the amplitude of events in signal-to-noise ratio units. The type of each event is determined by the method of Sect. 3.1. We can see that long glitch events are dominant at lower amplitudes, while short events dominate at higher amplitudes. The separation between short and long events is not efficient below about 20$\sigma$ (i.e., 20 times the rms noise), because the tails of long glitches, used to distinguish between the two types of events, are barely detectable. Nevertheless, we will see later that long glitches are dominant at lower amplitudes, as can be guessed by extrapolating the counts. Long glitches are dominant in the overall counts. The distribution of long glitches is well fitted by a steep power law of
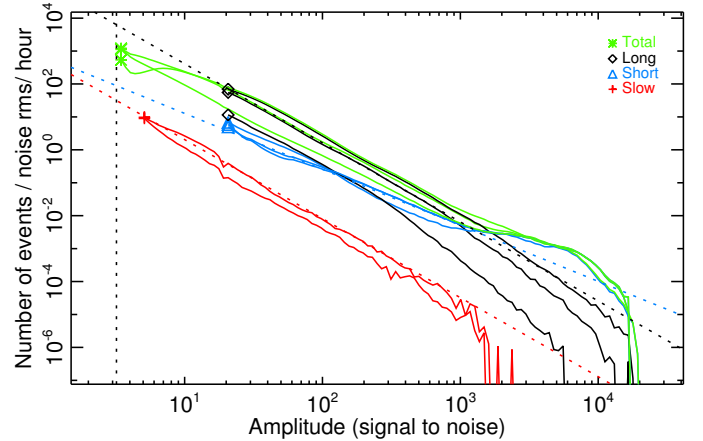


**Fig. 8.** Distributions, d$N$/d$E$, of the three families of glitches with respect to the peak amplitude, in signal-to-noise ratio units, for three different bolometers: 143-1a; 143-2a; and 217-1. The blue line is for the short glitch population, black is for long, red is for slow, and green is for total. We have chosen bolometers with very different behaviour: 143-1a has one of the lowest glitch rates while 143-2a and 217-1 have high glitch rates. The faint-end break of the glitch counts is visible for 217-1, a bolometer that has no slow glitches (see Sect. 2.3). Power laws are shown for comparison as dashed lines. Indices and amplitudes of power laws are chosen to match the distribution of bolometer 143-2a. Indices are $-2.4$ for long and slow glitches, and $-1.7$ for short glitches. The vertical dashed line indicates the detection threshold. There is no attempt here to separate the long and short glitch populations below 20 times the rms noise. The slow glitch spectrum is shown down to 5 times the rms.

index $-2.4$ between typical amplitudes of 20 and 1000 times the rms noise (with some variations among bolometers), and shows breaks at both the bright and faint ends. The faint-end break is close to the glitch detection threshold, which is fixed at 3.2$\sigma$, and is detected very significantly (as we will discuss in Sect. 5.4). The submillimetre channels (545 and 857 GHz) are more sensitive to long glitches. For those detectors, we observe a peak in the differential counts at energies close to the detection threshold. We will see in Sect. 5.4 that very few events are expected below the detection threshold. We observe a large scatter from bolometer to bolometer in the amplitude scaling of the long glitch distribution, but the overall shape is preserved.

The distribution of short glitches has a bump at amplitudes around 3000$\sigma$ for all bolometers from 100 to 353 GHz. There is a clear break at very high amplitudes, which is mostly due to the nonlinearity of the detectors at those amplitudes and to the saturation of the analogue-to-digital convertor (ADC, see Planck Collaboration VI 2014, for a discussion of the effect on the data). The bump in the distribution is not apparent in the submillimetre detectors, but this is due to the nonlinearity smearing it out. For amplitudes below about 1000$\sigma$, the distribution of short glitches is well represented by a power law with a typical index of $-1.7$. Short events with an energy corresponding to the bump appear to have shorter timescales than events corresponding to the power law.

The shapes of the distributions of slow and long glitches are very similar. We see in Fig. 8 that long glitches are more numerous than slow glitches, but the distributions shown are normalized to the peaks of events. After rescaling on the amplitude of the slow tails, which are similar for the two populations, the slow glitch distributions end up much closer to the long glitch
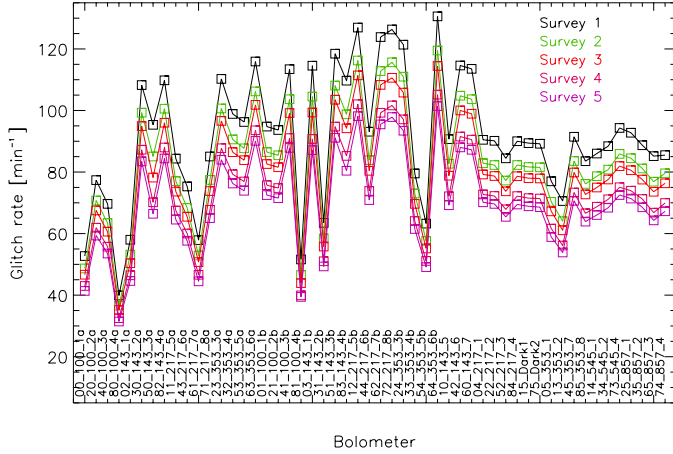
**Fig. 9.** Glitch rates for each bolometer. Points represent the mean values during each 6 month survey.

distributions. The slow glitches are then contributing very significantly to the noise power excess.

The glitch rates per bolometer are given in Fig. 9 for each six-month survey. Numbers are derived by integrating differential counts down to the detection threshold. Long glitches dominate the counts. Variations across bolometers are mainly explained by the differences in the sensitivity to long glitches. In particular, channels with lower rates also have more events below the detection threshold. As described in Holmes et al. (2008), bolometers in PSBs were selected from die on the same wafer. Also, attempts were made to select die from neighboring locations on that same wafer. In 14 of 16 PSBs, the PSB-a and -b are from the same wafer. Due to limited yield, for 2 of the 100 GHz PSBs, 100-2 and 100-4, PSB-a and PSB-b are from different wafers. Nevertheless, as shown in Fig. 9 there is no significant difference between the bolometers in these two PSBs compared to difference in bolometers in PSBs where both bolometers are from the same wafer.

## 3. Glitch detection and removal

Now that we have described the three glitch families, we focus on the detection and removal method. An earlier version was described in Planck HFI Core Team (2011b). Here, we summarize our approach and note the changes that have been implemented. We also demonstrate the efficiency of the method and show the impact on the noise power spectra.

### 3.1. Method

The technique for glitch removal iterates between sky signal estimation at the ring level and glitch detection and fitting. The iteration procedure, and the method used to estimate the sky signal for the first iteration, are presented in Planck HFI Core Team (2011b). Each ring is analysed independently (see Planck Collaboration I 2011, for the definition of a ring). A simple digital three-point filter (0.25, 0.5, 0.25) is used for glitch detection. This filter performs similarly to an optimal matched filter based on fast glitch shapes, since the bolometer time constant is very close to the sampling period. It has the additional advantage of reducing ringing around large events resulting from the electronic filter (Lamarre et al. 2010) and demodulation of the data. Depending on the ring, five to nine iterations between sky signal estimation and deglitching are necessary for convergence.

### 3.1.1. Glitch detection and template subtraction

After estimating the sky signal (as described in Sect. 3.1.3) at the previous iteration, and removing it from the data, events are detected by selecting local maxima in the three-point filtered data above a noise threshold set at $3.2\sigma$ on a sliding window of 1000 samples[2]. On each window, a joint fit of the amplitudes of short and long glitch templates is performed simultaneously for all detected events in the window, centred at the maximum event. The short and long glitch templates are built independently, and each is a sum of exponentials, three terms for short and four terms for long glitches. Templates are estimated by stacking events detected and separated into categories by earlier versions of the same method. The parameters of the templates are essentially independent of the changes in the method, since templates are determined using the list of detected high energy glitches, which is not sensitive to the details of the processing, and it was not necessary to iterate the glitch template estimation. The method used to estimate the templates is described in Sect. 3.1.4. The joint template fitting of both short and long glitches is a significant improvement over the method used previously (Planck HFI Core Team 2011b). It has improved the accuracy of determination of the long glitch template amplitude and led to smaller glitch residuals in the final noise. Only one overall amplitude is used as a free parameter for each glitch type and for each event.

Detected glitches are fit to the templates starting from three samples after the maximum for small-amplitude glitches in PSB-b or SWB detectors, increasing to eight samples after the maximum for large-amplitude glitches, and from six to eight samples in PSB-a detectors (because of the presence of slow glitches). In order to break degeneracies between template amplitudes in the case of high confusion between events, we use the prior that amplitudes are positive. The parameter fitting is performed by analytical minimization of $\chi^2$, as detailed in Eq. (2) of Planck HFI Core Team (2011b). Two parameters per event are fitted: the amplitudes of the long and short glitch tails described by the two templates. Priors are implemented by setting parameters that fall outside the allowed range to fixed values; in particular, negative amplitudes are replaced by zeros, and then another minimization is performed.

Slow glitches are detected as long glitches with extremely large amplitudes. Thus such events are processed in the same way as long glitches but with higher fitted amplitudes relative to the peak. When a slow event is detected, another iteration of the $\chi^2$ minimization is performed, in which the long template is adapted by removing the fastest exponential.

If the measured long glitch template amplitude for an event in the vicinity of the largest event is above the threshold (fixed to 0.5 times the expected amplitude for a long glitch at the measured peak amplitude), then the long glitch template is removed from the data. The expected amplitude of the long glitch tail accounts for the nonlinearity described in Sect. 2.2; we use a simple empirical quadratic law, which is fitted to the data, relating the glitch template amplitude and the peak amplitude. To remove the template from the data, we use the fitted value of the amplitude of the long glitch template for events above $10\sigma$. Glitches with overall amplitude below $10\sigma$ are treated either as long or slow glitches, and the amplitude is fixed to the expected values. This is because the long glitches dominate at low amplitude, and because the fitting errors are larger than the model uncertainties.

---

[2] The choice of $3.2\sigma$ is a compromise between false event detection and completeness of glitch detection (Planck HFI Core Team 2011b, see Fig. 7).

The fitted short glitch template is not removed from the data (this has no impact on the data as discussed later): affected data are just flagged.

### 3.1.2. Data flagging

For long and slow events, data are flagged in the vicinity of the peak when the fitted long glitch template is above three times the rms noise, and the flagged samples are not used for scientific analysis (or for fitting the next event). For events belonging to the short category, or at least detected as such, i.e., for which the fitted long glitch template amplitude is below the detection threshold, data for which the short glitch template is above $0.1\sigma$ are flagged.

At the end of the glitch detection and subtraction procedure, a matched filter, optimized to detect 2 s exponential decays, is applied to the data, in order to find events that are missed by the method, or events for which the fit failed. This introduces an extra flagging of about 0.1% of the data. Additional glitch cleaning and the use of different adaptive filters were not found to improve the data any further.

### 3.1.3. Sky subtraction

The sky signal is estimated at each iteration on each fixed pointing period (ring), detector by detector, and this is done independently using the redundancies of the measurements. Third-order spline coefficients are fit to nodes separated by $1'.5$ to account for subpixel variations, which could otherwise be detected as glitch signals. Flags set during previous iterations are used to reject data, and estimates of the long glitch templates are removed prior to the sky signal estimation.

Special sky estimation and glitch removal procedures are required when scanning through or near bright objects, including planets and bright sources in the Galactic plane. This is to account for systematic errors in the subtraction of the sky signal that could be falsely flagged as glitches. These errors are mainly due to two effects: slow cross-scan variations of the pointing within the ring scan time, yielding pointing uncertainties of the order of a few seconds of arc (Planck Collaboration VI 2014); and subpixel variations that are not entirely captured by the spline coefficients.

For rings with large signal in the Galactic plane, we add to the noise variance the square of a term representing the signal reconstruction error, which is 1% of the signal for submillimetre channels (545 and 857 GHz) and 0.5% for the other channels. This automatically increases the threshold used for glitch detection for bright regions of the sky. Also, long glitch templates are not removed for high sky signals. This correction of the threshold is effective for all rings for the submillimetre channels, but only applies to a few percent of the data close to the Galactic centre for the other channels (see Planck HFI Core Team 2011b). Further special treatment is required to process the data on bright planets. The motions of planets during one hour on the sky (which are mainly cross-scan) and the cross-scan pointing uncertainties are both accounted for. We fit the amplitude of the planet signal for each scan, rescale the averaged signal estimate on the ring using the estimated amplitude coefficient to reconstruct the sky signal, and remove the best estimate of it from the data. This procedure neglects main-lobe beam asymmetries. However, we find that it is a good approximation at this stage, given the small cross-scan shift of the planet signal during the time taken to scan one ring.

Sky signal estimation and glitch detection and subtraction on each ring are iterated until the results converge to sufficient accuracy. For most rings, six iterations are necessary (see Planck HFI Core Team 2011b).

### 3.1.4. Template estimation

Long and short glitch templates, built from a sum of exponentials, are fitted to stacked (normalized and averaged) large amplitude events (typically 1000 times the rms noise). Any representation of the glitch pulses providing a good fit to the stacked glitch data would have been convenient for the analysis. However, the functional form is motivated by very simple physical thermal models of the bolometer and its environment. Time series are not used directly because of noise contribution to the long tail which is filtered by the model. The stacked data are produced using the median value for each bin corresponding to the sampling period index after the maximum. The median is used to avoid significant contribution from other glitches. Figure 10 shows the difference between long glitch stacks and the best-fit template (with four exponentials) in different energy windows for one bolometer (143-3a). The glitch template is determined using events with amplitudes between 1200 and $2400\sigma$.

The difference between the stacked glitch data and the fitted template is small, but not consistent with zero, reflecting the limit of the summed exponential model. The difference is systematic, has a low frequency component, and is about 1% of the template, which is much smaller than the fitting errors in each individual glitch described in Sect. 4.2.2 (see Fig. 16 in particular). We therefore expect that the impact of this inaccuracy on the final results is negligible. We see no evidence for significant variations of the shape of the template with the amplitude of the glitch, over a wide range of amplitudes: the difference between the glitch template and the stacks computed over different ranges of glitch amplitude, between 300 and $5000\sigma$ (after correcting for the nonlinearity of the glitch tail amplitude relative to the peak described in Sect. 2.2), is no larger than in the amplitude range of $1200$–$2400\sigma$ where the template is fitted. The template used for the analysis has been estimated for a limited range of energies to avoid mismatch due to the nonlinearity effects.

For small glitches, with amplitudes $<300\sigma$, there is a non-negligible difference between the stacked glitches and the fitted template. This is attributed to strong selection biases, e.g., Eddington-type bias, which affects the stacked signal, and not to real variations of the glitch template. This bias is clearly observed for stacked samples, showing a difference in the mean offset before the events compared with after the events (measured a few tenths of a second later, when the glitch tail is negligible). This bias is expected to be small for the high-amplitude events used for modelling the templates.

### 3.2. Results

The fraction of the data that are found to be contaminated by glitches and are ignored in the analysis varies from 6% (for detectors with fewer long glitches) to 20%, depending on the bolometer. The averaged fraction of flagged data by HFI frequency is 14.4, 16.1, 16.8, 17.1, 12.8, and 11.2%, for 100 to 857 GHz. Figure 11 shows a segment of data for a bolometer with a high glitch rate after glitch template subtraction. This is the same segment as shown in Fig. 3 before deglitching. It shows clearly that the template subtraction is very effective.
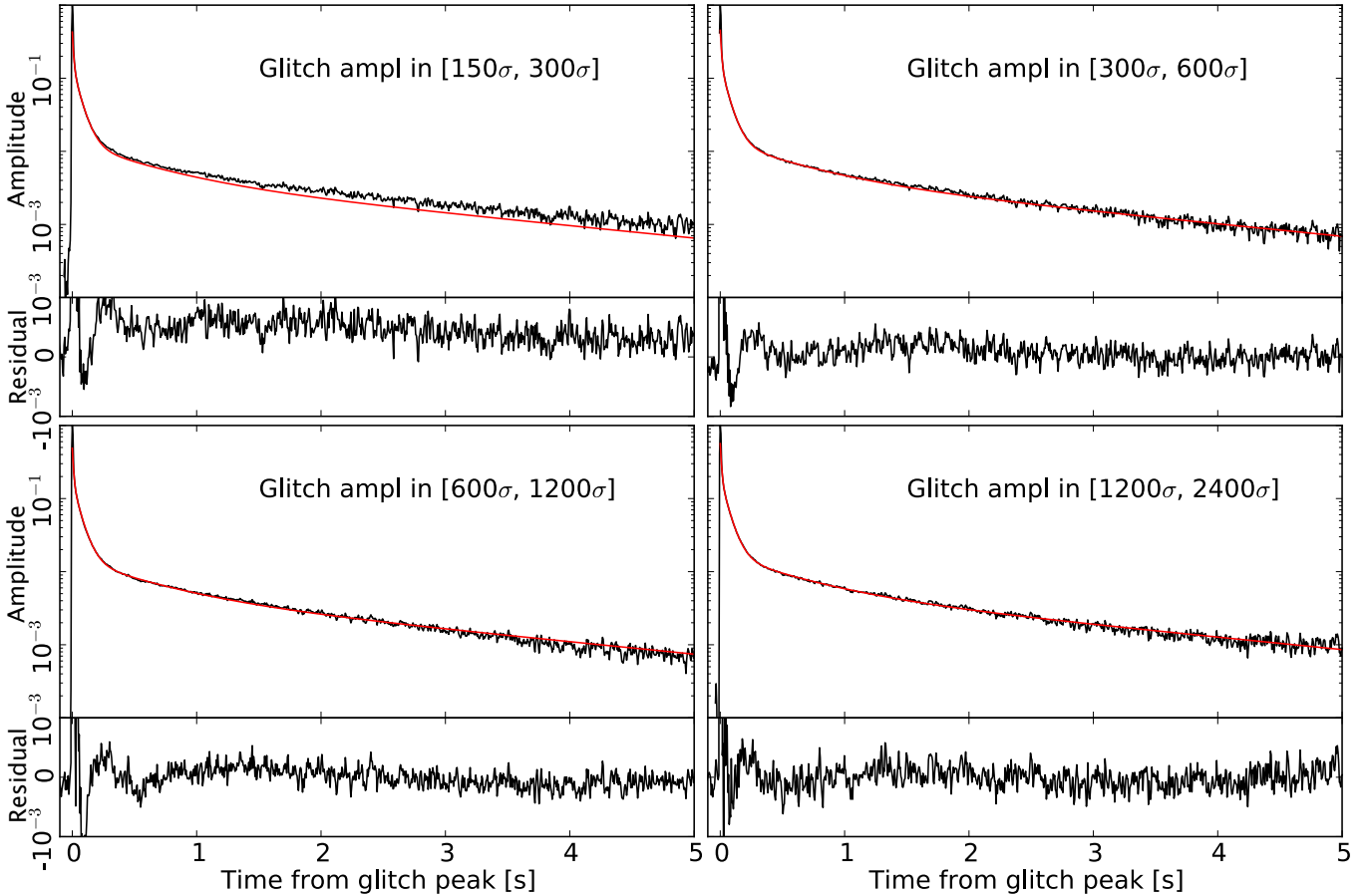
**Fig. 10.** Stacking of long glitches of bolometer 143-3a in different energy windows, after normalizing each event to the maximum amplitude. The solid lines show the long glitch template obtained after fitting four exponentials, using the data shown in the *lower right panel*. Templates are rescaled in amplitude in each pannel to match the stacked data due to the nonlinearity of the long glitch tail relative to the peak presented in Sect. 2.2. In each panel the lower curve shows the difference between the stacked data and the template. There is good agreement between the template and the stacked data, typically within 1%.
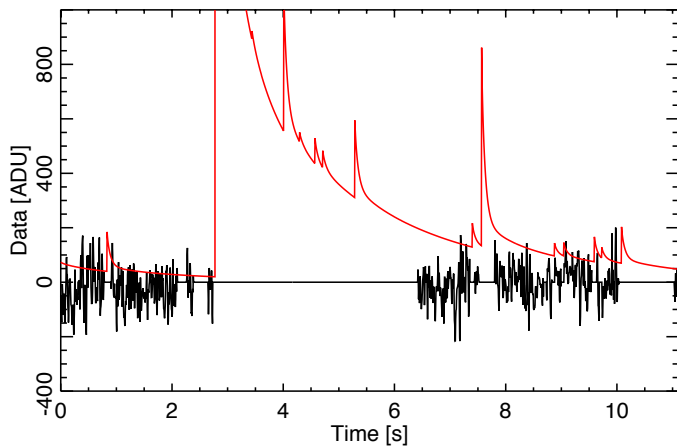


**Fig. 11.** Segment of data for one detector at 143 GHz after long glitch template subtraction. The same segment before template subtraction and flagging is shown in Fig. 3. An estimate of the sky signal has been subtracted. The time stream reconstructed from the estimated templates of long glitches that have been subtracted from the data is shown in red. The flagged data that are not used for scientific analysis are set to zero.

The subtraction of long and slow glitch templates significantly reduces the contamination of the cosmological and astrophysical signal. Figure 12 compares the power spectra of noise with and without glitch template subtraction. The power spectra are computed after sky subtraction (only the part of the noise that does not project onto the sky is left), from raw three-point filtered data (same filter as applied to the data prior to sky signal estimation and deglitching), for all the detectors from 100 to 353 GHz that are used for cosmology. Both data sets were flagged in the same way after glitch detection, gaps were filled with white noise plus low frequency noise estimated from smoothing data with a Gaussian. Power spectra are computed on data chunks of size corresponding to about 100 rings, which are averaged over the period covered by the nominal mission. An estimate of the sky signal has been previously removed ring by ring for each bolometer using redundancies, as described in Sect. 3.1, and after subtracting the averaged signal for each ring, to avoid filtering the noise on timescales larger than the ring scale. Before correction, the power spectra are highly contaminated by glitches at frequencies between 0.002 Hz and 2 Hz. The 2 s tail is responsible for the excess between 0.01 and 0.1 Hz, while the intermediate time constant of 50 ms produces an excess around 0.4 Hz, explaining why PSB-a detectors have a higher relative excess at that frequency. We observe a large reduction of the residual noise after template subtraction. Some detectors have very low contamination from long glitches; this is the case for 143-5 and 143-1a, which correspond to the two lowest spectra before correction (top right panel of Fig. 12). The
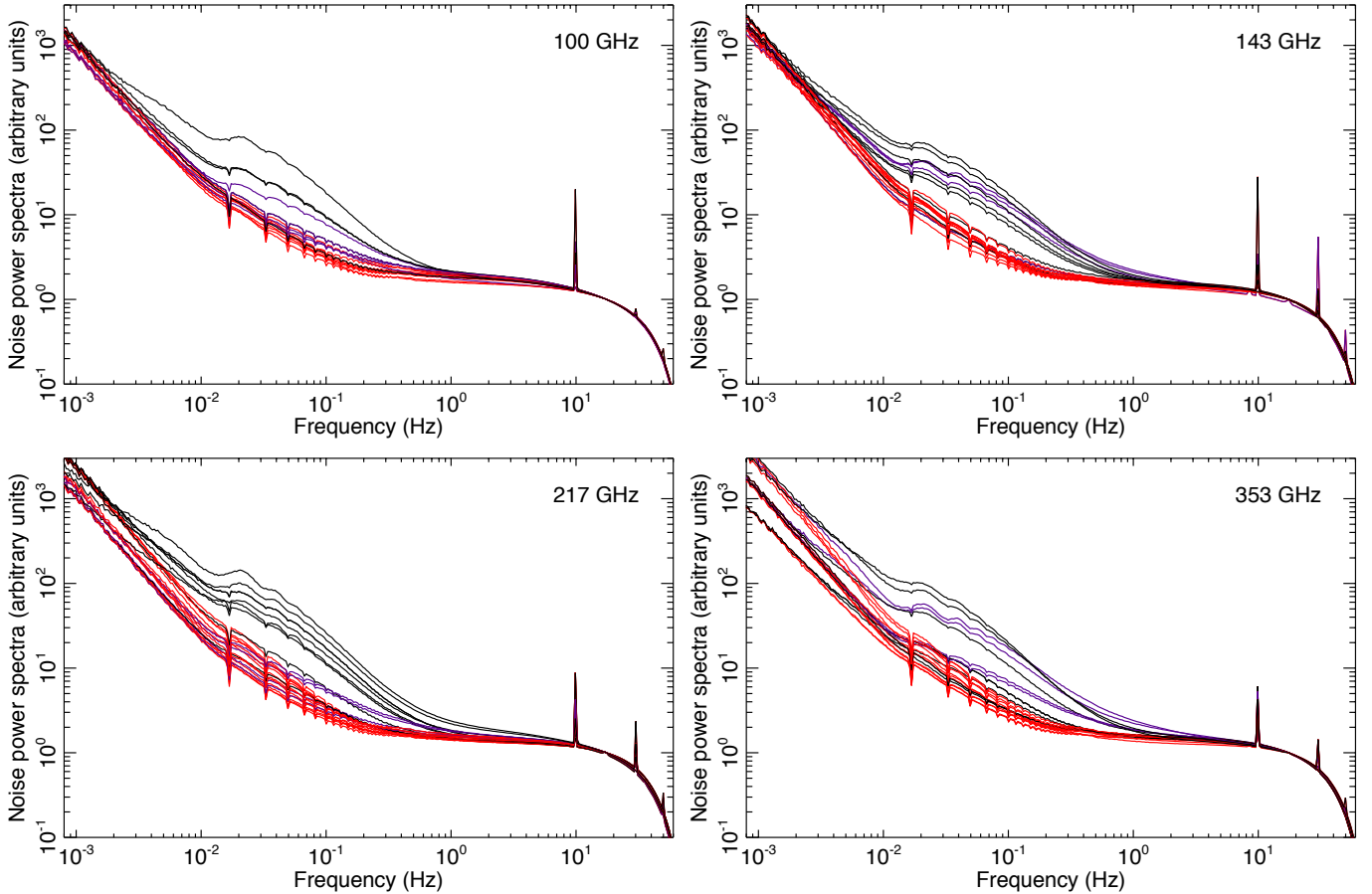
**Fig. 12.** Power spectra of the component of noise that does not project onto the sky, for each bolometer at frequencies between 100 GHz (*top left panel*) and 353 GHz (*bottom right panel*). Black curves correspond to the power spectra without subtraction of templates for PSB-b and SWB detectors, while the blue curves are for PSB-a detectors. Power spectra are rescaled in amplitude so that they all match at 20 Hz. The red curves are with template subtraction. Power spectra are computed over subsets of about 100 rings and are averaged over the nominal mission. The sky signal has been previously subtracted from the data. This creates the narrow dips in the spectra at the harmonics of the spin frequency. Data have also been three-point filtered and flagged after glitch detection. The large spikes in the spectra, unsubtracted at this stage, are induced by the 4 K J-T cooler and are described in Planck Collaboration VI (2014). The roll-off of the spectra above 10 Hz is mainly due to the three-point filter. Glitches contribute to the power spectra between 0.002 Hz and 2 Hz. The power spectra of residual contamination is significantly reduced after glitch template subtraction, at frequencies below a few hertz. There is much less dispersion between the power spectra from different detectors after correction – less than a factor of two – indicating that contamination from remaining glitches is not a dominant effect.

improvement after deglitching is effective but small for these detectors, as expected, and their corrected power spectra are very close to the fundamental limit of the noise. The power spectra for these detectors are then indicative of the power spectra of noise without glitches. The power spectra for the other detectors approach this limit after template subtraction. Noting that the $1/f$ part of the spectrum varies in amplitude from bolometer to bolometer, we conclude that residual contamination from glitches is below the noise level at all scales for all detectors.

One and only one of the 100 GHz bolometers (100-1a) has an extra family of glitches that are not properly accounted for by our deglitching method. Some of these events are detected as "long" in the processing, and then the long glitch template is incorrectly subtracted (those events are shorter than the long events). But the matched filter, designed to detect long glitch tails (either positive or negative) allows us to flag segments of data when this happens, limiting the effect. This bolometer is the one with the largest excess noise power at frequencies around 0.1 Hz. This is still a small effect, which is accounted for in the total noise budget (Planck Collaboration VI 2014).

The power spectra of noise after sky subtraction are indicative of the quality of the glitch correction, but cannot be used

to derive accurately the contribution to the maps. The reason is that part of the noise is filtered due to the "noisy" estimation of templates by the fitting procedure, which are then removed from the data. This is not the case for the signal projecting onto the sky, since the method iterates between sky signal and glitch detection, and then template fitting and subtraction. The contribution of glitches to the total power after data reduction at the map level, and at the ring level, can be studied with simulations (Sect. 4).

As we will see in Sect. 5.4, long glitches occur simultaneously in both bolometers of a PSB pair. Consequently, glitches below the detection threshold, or any unsubtracted tails, are expected to induce residual additional correlations between bolometer time streams from the same pair. In order to evaluate the contribution from residual glitches we have computed the cross-power spectra between bolometers. These are shown in Fig. 13 for detectors at 100 GHz, after averaging cross- and auto-power spectra computed on data segments of about 100 rings over the entire nominal mission. The sky signal has been removed and data have been processed in the same way as previously described for auto-spectra. Bolometers from the same PSB pair have an extra correlation above 0.2 Hz, which
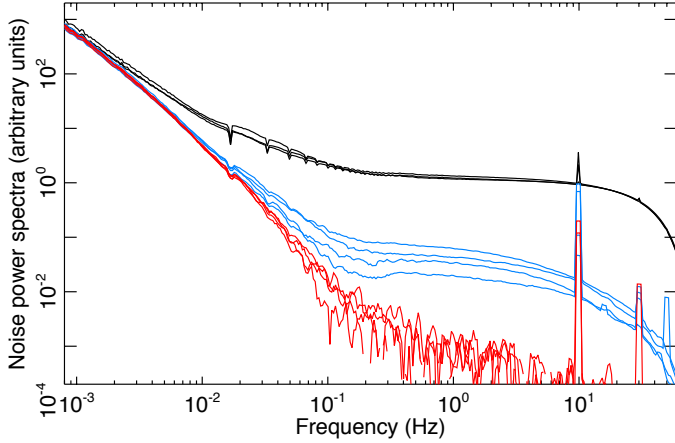
**Fig. 13.** Cross- and auto-power spectra between detectors at 100 GHz. Spectra are computed in the same way as described in the caption of Fig. 12. Black curves correspond to some of the auto-spectra shown in the same figure. Data have been rescaled so that auto-spectra match at 20 Hz, and so that the white noise level is approximately unity. Blue curves correspond to cross-spectra between detectors from the same pair. Red curves are for detectors from different pairs. The extra correlation observed for PSB pair bolometers, above 0.1 Hz and at the level of 2 to 7% of the white noise spectrum, is due to residual glitches below the threshold. Some residual correlation at the level of about 0.1% at 0.2 Hz can be seen between other bolometer pairs that are spatially close to each other; this might result from imperfect sky signal subtraction due to pointing drift, since the error is coherent between different nearby detectors. The low frequency noise is highly correlated between detectors and is due to thermal fluctuations of the focal plane. The level of correlation of the 4 K lines in the plot is not representative of the residual obtained after the TOI processing.

is around 2–7% of the white noise level in the spectrum for 100 GHz bolometers. The correlation is 2–3% for PSB pairs at 143 GHz, 1–4% at 217 GHz, and 2–4% at 353 GHz. Simulations presented in the next section show that the residual noise excess is of the order of 5% (Fig. 16); given our modelling of glitches (Sect. 5.4), and noting that about half of the glitches have the same amplitude in PSB-a and PSB-b detectors (see Sect. 5.4), we should have roughly 5% correlation in the noise spectrum. This is slightly higher than the 3% observed for this pair. The difference could be due to uncertainties in our modelling and model extrapolations. It is important to note that we observe stronger correlations in pairs for which both detectors have few detected long glitches, e.g., the 100-4a/4b pair, for which the detectors have the lowest glitch rates (as shown in Fig. 9), and which have 7% cross-correlation (as seen in Fig. 13), the highest observed for any pair. This is entirely explained by the fact that both detectors then have more glitches below the detection threshold, since the counts for long glitches are similar between detectors, but are essentially scaled in energy, as described in Sect. 5.4. By contrast, pairs for which the faint-end break in counts is above the detection threshold have significantly lower correlations above 0.1 Hz.

We have shown that glitches below the detection threshold are responsible for the extra correlation in the noise by averaging the two time streams from each pair of bolometers, and looking for events above $3.2\sigma$ (of the noise) in the combined data. This allows us to detect coincident glitches with amplitudes lower by a factor of $\sqrt{2}$ for about half of the events, enabling us to divide the correlated noise by a factor of 2, with only 0.1% of additional data flagging. This shows, without ambiguity, that the

extra correlation between two bolometers in PSB pairs is due to undetected long glitches below the threshold.

Furthermore, this analysis confirms that the number of undetected glitches is small and that a change in slope (or break) must happen in the counts close to the detection threshold, as we would otherwise have expected more correlations in the noise between PSB pairs. Those glitches then account for a small fraction of the total noise power.

## 4. Impact of glitch residuals on final results

### 4.1. Simulations

In order to estimate the contamination from glitches that remains after processing, we have performed simulations of glitch time streams, incorporating the glitch properties that we measure in data. The simulations include the following features.

– Glitches are generated using a Poisson distribution, with sub-sample resolution.
– Generated glitches follow the population spectra that are found in data for each population by combining bolometers, and using the model explained in Sect. 5. Population spectra are rescaled in energy for each bolometer to match the measured counts. In particular, we use to build the model the measured number counts of long glitches in the submillimetre channels because those channel are more sensitive to low-energy glitches, below the faint-end break. Population spectra of short and slow glitches are extrapolated at low energy (for which events can not be detected individually) using power laws.
– The nonlinearity of the slow tail of long glitches relative to the peak amplitude is included (see Sect. 2.2 for details).
– The temporal shape of glitches is simulated using templates for the slow parts (after about 20 ms), analytically correcting the effect of the sampling average and of the three-point filter on the amplitude of the exponentials, since those are applied to the data before template estimation. The fast part of glitches is simulated using subsample resolution, and then averaged over the sample period with a simple boxcar average.

The simulations do not include the apparent scatter of the slow tail amplitude of long glitches, apart from the intrinsic scatter due to the variations of the arrival time in the sample period. Those fluctuations do not strongly affect the performance of the method, since the slow part of the glitches is fitted before subtraction, and so the amplitude variations are absorbed by the fit. Moreover, we used a fixed template for short glitches, which is not completely realistic, since we have observed scatter in the slow tail, and we have identified two subcategories of short glitches. The effect of using a single, fixed template for short glitches should be very small, since the short glitch templates are not removed. We did not include the 2 s exponential decay for short glitches in the simulations, since the uncertainty in its amplitude is large. Nevertheless, we estimate that the contribution to the power spectrum should be below 0.1% of the noise power spectrum, given the distribution of short glitches. The effects of nonlinearity of the bolometers and the ADC are not simulated. The nonlinearity has the effect of reducing the fast part of the glitches, which dominates at very high amplitudes. We do not expect this to degrade the performance of the method for the slow part of the glitches, since the template fitting starts a few samples after the peak, in a part of the signal that is not
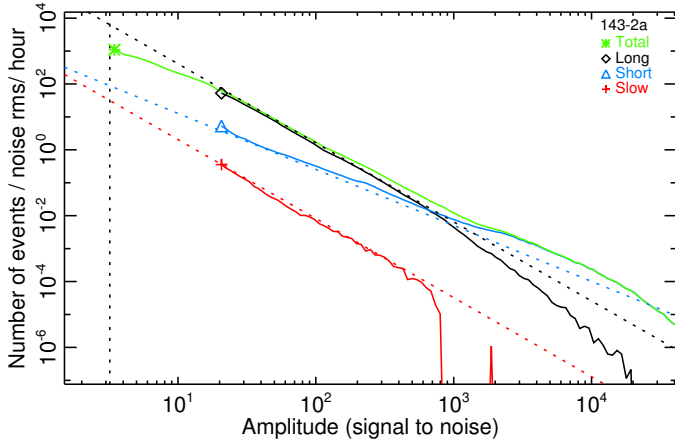
**Fig. 14.** Differential counts for the three populations of glitches for one of the detectors with a high rate of glitches (143-2a) measured from simulated data. This can be compared to the results on real data shown in Fig. 8 for the same bolometer. Dashed lines are shown for reference and are identical to the lines shown for the real data. There is almost perfect agreement between simulations and data, except for very high amplitude glitches $\gtrsim 10^4 \sigma$. Those glitches are affected by the bolometer nonlinearity in the real data, an effect that we did not simulate at this stage, explaining the discrepancies in the counts. We simulated slightly fewer very high amplitude slow glitches than in the *Planck* data. This affects only about one event per day.

affected by nonlinearity. Finally, we do not include the correlation of glitches between PSB pairs, but treat each bolometer independently.

To the generated glitch signal, we add Gaussian noise containing a white component and a low frequency component described by a power law fitted to the data (with an index and $f_{\mathrm{knee}}$ parameter). We also add a time stream of pure signal obtained by scanning over a simulated cosmic microwave background (CMB) map, as well as Galactic dust and point source maps from the *Planck* Sky Model (Delabrouille et al. 2013), using the pointing solution derived for the actual data. The constructed signal time stream is formed by interpolating the extracted signal from the map to limit subpixel effects (see Reinecke et al. 2006, for the methodology). We also filter the simulated data using the same three-point filter as used for the data. The differential counts recovered from the simulations after processing are shown in Fig. 14 for bolometer 143-2a. There is very good agreement with the spectra recovered in *Planck* bolometer data, shown in Fig. 8.

### 4.2. Error estimation

#### 4.2.1. Evaluation of signal bias due to the deglitching procedure

Due to the high signal-to-noise ratio of HFI data, the sky signal subtraction is a critical part of the deglitching procedure. Errors in the sky signal estimation could easily induce spurious detection of glitches and errors in the template subtraction, which would then correlate with the signal. This could bias the sky signal estimation for two main reasons: first by flagging data as bad slightly more often on average when the sky signal is higher (or lower); and second, by subtracting slightly more glitch template signals when the fluctuations of the sky signal are of a given sign.

We have verified the absence of bias in the signal with the help of simulations. Specifically, we have computed signal rings

by projecting pure signal time streams used for simulations, which we write as $r_{0i}(p)$, where $p$ is the ring pixel and $i$ is the ring number. We have also projected the simulated observed data from which we have subtracted estimated glitch templates, after applying the deglitching procedure used for real data and rejecting flagged data. We write this last quantity as $\hat{r}_i(p)$ for data ring $i$. We then computed the average binned power spectrum of $r_{0i}(p)$ as:

$$P_0(q) = \frac{1}{NN_q} \sum_{i=1}^{N} \sum_{k \in D_q} r_{0i}(k)\, r_{0i}(k)^\dagger, \tag{1}$$

where $\dagger$ denotes the transpose conjugate, $r_{0i}(k)$ is the Fourier transform of $r_{0i}(p)$, $D_q$ and $N_q$ are the intervals in $k$ and the number of modes in bin $q$, respectively, and we have summed over $N$ rings (with $N$ of the order of $10\,000$). We also computed the average cross-power spectrum between $r_{0i}(p)$ and $\hat{r}_i(p)$ as

$$P_{\mathrm{c}}(q) = \frac{1}{NN_q} \sum_{i=1}^{N} \sum_{k \in D_q} r_{0i}(k)\, \hat{r}_i(k)^\dagger. \tag{2}$$

In the absence of bias in the signal introduced by any of the two effects previously described, $P_{\mathrm{c}}(q)$ should be an unbiased estimate of $P_0(q)$, i.e.,

$$P_0(q) = \langle P_{\mathrm{c}}(q) \rangle, \tag{3}$$

where $\langle \cdot \rangle$ is the ensemble average over an infinite number of realizations of noise and glitches.

In practice, the quantities $P_0(q)$ and $P_{\mathrm{c}}(q) - P_0(q)$ are evaluated for simulations of the 143-2a detector for $N = 10\,000$ rings. We selected rings with no strong Galactic signal, to avoid giving too much weight to the Galaxy, keeping about 95% of the rings. Results are shown in Fig. 15 for logarithmically spaced bins. We can see that $P_{\mathrm{c}}(q) - P_0(q)$ is compatible with zero at all scales. We estimate an upper limit to the bias of around $5 \times 10^{-4}$ in individual bins at all scales relevant for cosmology, i.e., for $k$ corresponding to $1 \le \ell \le 2000$. The absence of significant bias due to the deglitching procedure is verified at the ring level, but this conclusion can be drawn at the map level, and hence at the CMB power spectrum level. Also, we do not expect to observe differences for the CMB measured with other bolometers, since the presence of bias has to do with the errors made in the sky signal reconstruction, and not on errors made in glitch template fitting and subtraction. Nevertheless, we have performed the same exercise for an SWB bolometer at 143 GHz (143-5). We did not find any bias and can place an even lower limit of $2 \times 10^{-4}$, due to the lower rate of glitches for this bolometer.

The situation is different for strong Galactic signals and for high frequency channels, since the detection threshold is increased with the signal amplitude and even long glitch templates are not subtracted for very high sky signal, as described in Sect. 3.1. We expect this to slightly bias the estimation of the sky signal in the positive direction, since less positive glitch signal is removed in regions of strong sky signal. This effect is described in detail in Planck HFI Core Team (2011b). In particular we observed an effect of the order of $4 \times 10^{-4}$ of the signal amplitude at 545 GHz. The effect on the beam response estimation is studied in detail in Planck Collaboration VII (2014).

Because the sky signal is estimated using data from individual rings, the estimate is noisy, with an rms that is reduced by roughly a factor of 7 compared to the rms of the noise in each measurement. This induces some weak correlations in the glitch detection between each circle in the ring, after the sky signal has been removed from the data. However, this effect does
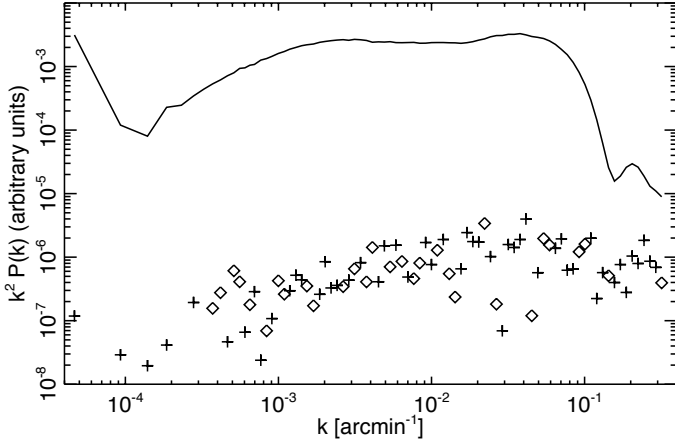
**Fig. 15.** Constraints on the signal bias after deglitching. The black curve is the power spectrum ($k^2 P_0(k)$), with $k$ taken at the centre of each bin $q$) of ring data after projecting a pure simulated signal time stream for one detector, containing CMB anisotropies, Galactic dust and point source signal, and using the actual pointing. For the other displayed points we computed the cross-spectrum between: (1) the estimated signal on rings after subtracting long glitch templates from the simulated data and after flagging; and (2) the input signal only averaged on the same rings. Crosses and diamonds correspond to the difference between this cross-spectrum and the pure input signal power spectrum shown in black, for positive and negative points, respectively. The quantity displayed is $k^2(P_c(k) - P_0(k))$. We averaged the power spectra of 10 000 rings. Simulations were performed for detector 143-2a which has a high glitch rate. In the absence of bias in the signal due to the deglitching, we expect that the cross-power spectrum is an unbiased estimator of the input signal power spectra, and that the difference should then be compatible with zero. We do not detect significant bias in any of the 100 logarithmically spaced bins, and we place an upper limit of $5 \times 10^{-4}$ on each bin at the scales relevant for CMB analysis.

not bias the estimation of the signal, as shown above, but correlates slightly, at the level of 1%, with the remaining noise (after flagging and template subtraction) between subsets of data measured by taking half rings. We have studied this effect in Planck Collaboration VI (2014, see Table 2 and Fig. 32) and it has been taken into account for the noise prediction.

### 4.2.2. Residual glitch contamination

For some representative bolometers we have evaluated the level of contamination coming from glitches left in the data after processing at the ring level, by comparing the power spectrum of the input simulated noise projected on rings with the power spectrum of processed simulated data, after removing the input sky signal from the data. This is shown in Fig. 16 for simulations of data from the same two detectors as in the previous section: 143-2a, containing a high rate of long glitches; and 143-5, with a low glitch rate, but consequently more glitches below the threshold (see Sect. 5.4), after averaging the spectra over 10 000 rings. We also compare these two power spectra with the power spectra obtained without removing glitch templates from the data, but using the same data flagging.

For bolometer 143-2a, we can see that without template subtraction the glitch signal dominates over the noise on large scales, $k < 2 \times 10^{-3}$ arcmin$^{-1}$, even after flagging. We observe a dramatic improvement in the noise power spectrum after removing long glitch templates. Nevertheless, glitch residuals still contribute to the noise power at the level of 30%

at $k \lesssim 2 \times 10^{-3}$ arcmin$^{-1}$ and less than 10% at $k \gtrsim 6 \times 10^{-3}$ arcmin$^{-1}$. We attribute the excess at low frequency to errors in the subtraction of templates, which are expected to arise due to uncertainties in the amplitude parameter determination after $\chi^2$ minimization. Given the level of residuals in power spectra, the impact of errors in template estimation is negligible at the percent level, as seen in Sect. 3.1.4. Undetected glitches below the threshold contribute significantly at higher frequencies, at the level of 5% of the power for this bolometer, and cause the observed excess over $0.03 < k < 0.1$ arcmin$^{-1}$. For bolometer 143-5, the contamination by glitches before template subtraction below $k < 10^{-3}$ arcmin$^{-1}$ is between 15 and 20% and of the order of 8% above $10^{-3}$ arcmin$^{-1}$. After glitch template subtraction, the contamination reaches the level of 8% for almost all scales. This value corresponds to the level of contamination by undetected glitches below the threshold, which is higher than for the 143-2a bolometer, in agreement with our modelling (see Sect. 5.4).

This study shows that the remaining contamination from glitches is below the instrumental noise level, even for the channels with the highest glitch rates. Evaluation of the contamination at the map level and its effect on the CMB power spectrum is postponed until the release of the data for the full *Planck* mission. Nevertheless, the contribution of glitches to the errors on cosmological results (Planck Collaboration XVI 2014; Planck Collaboration XV 2014) has already been accounted for, since the noise estimation is based on differences of half-ring periods (Planck Collaboration VI 2014).

## 5. Glitch characterization and interpretation

In this section we focus on a more detailed description of the characteristics of the different glitch types and provide an interpretation of their origin. This analysis is complementary to the study based on ground tests presented in Catalano et al. (2014).

### 5.1. Evolution of the glitch rate over the mission

Over the course of the whole mission, the rates of each type of glitch decreased (Fig. 17). This decrease is universal for all bolometers (Fig. 9). The signal from diode sensor TC2, the most shielded of the three diodes in the standard radiation event monitor (SREM, Mohammadzadeh et al. 2003) located on the Sun side of the *Planck* spacecraft, follows a similar trend with time (Fig. 18). This trend is expected for Galactic cosmic rays modulated by the heliosphere of the Sun (Gleeson & Axford 1968; Bobik et al. 2012) and is observed by ground stations on Earth and other spacecraft in the solar system (Usokin et al. 2011; Wiedenbeck et al. 2005; Adriana 2011). Taking together the glitch rate, the SREM diode signal, and data from other studies, it is clear that the source of glitches in the HFI bolometers is dominated by Galactic cosmic rays. Indeed, other sources, such as on-board radioactivity and solar protons (as detected by the mirror on WMAP, Jarosik et al. 2007), were suspected to contribute to the glitch rate, but would not follow the trends with time that are observed.

### 5.2. Correlation in time

The time interval between two consecutive glitch events exhibits an exponential distribution (left panel of Fig. 19). The absolute value of the slope fitted between 1 and 2 min is roughly equal to the computed rate, simply obtained as the number of events
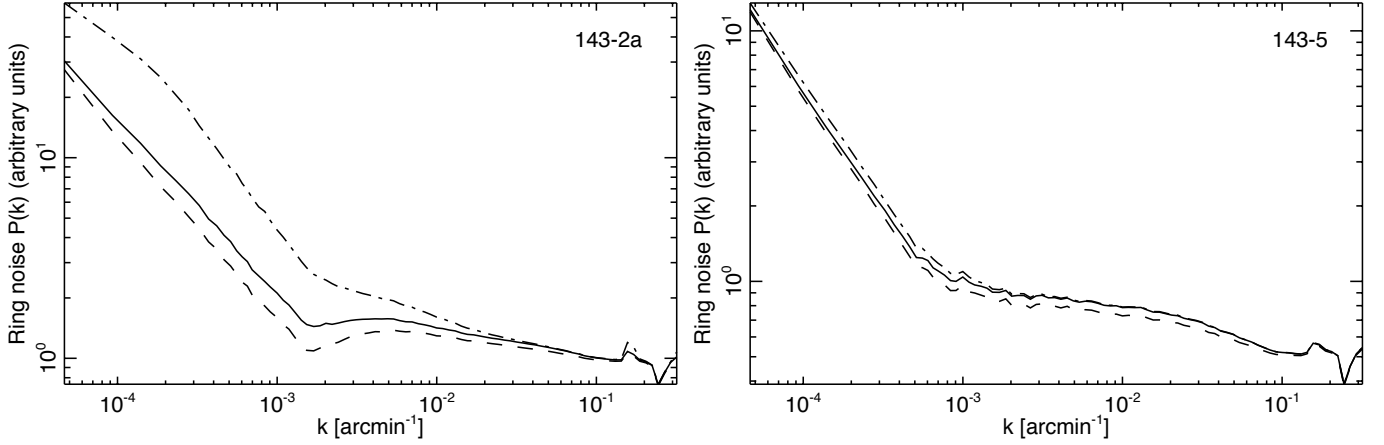
**Fig. 16.** Estimation of the power spectra of noise residuals after averaging data on rings for the 143-2a bolometer (*left*) and the 143-5 bolometer (*right*). Power spectra are averaged over 10 000 rings and are computed after removing the input simulated signal from the simulated data and using the estimated flags. The dot-dashed curve is the result without subtraction of long glitch tails, while the solid curve is with subtraction as done for the real data, and the dashed curve is for the same simulations but without glitches. Residual glitches are significantly reduced after template subtraction.
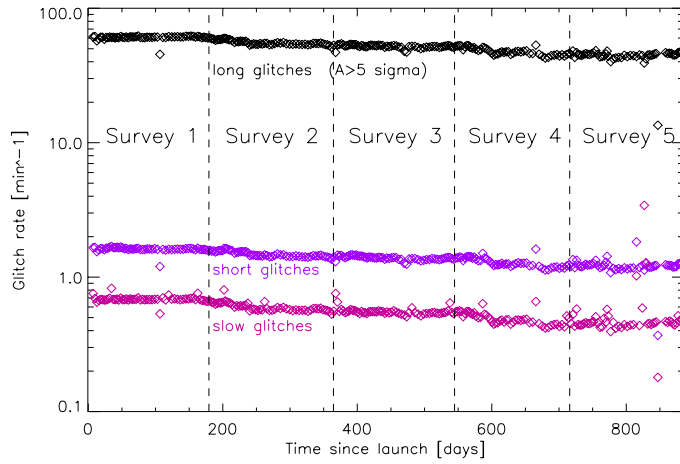


**Fig. 17.** Mean rate of the three categories of glitches, i.e., long, short, and slow. These rates are computed using all 52 bolometers for long and short glitches, and the 16 PSB-a bolometers for slow glitches.
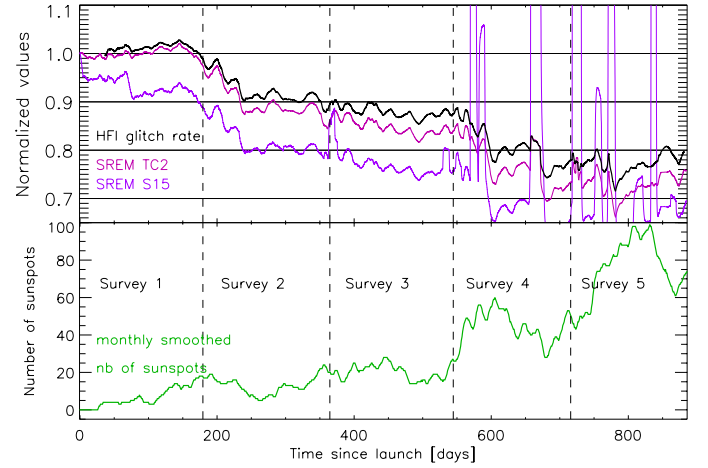
**Fig. 18.** *Top*: normalized glitch rate (black line), cosmic ray flux measured by the SREM for deposited energy $E > 3$ MeV (purple), and $E > 0.085$ MeV (pink), as a function of time. *Bottom*: monthly smoothed number of sunspots.

above $10\sigma$ in six months (right panel of Fig. 19). Clearly, all the bolometer glitch distributions exhibit Poisson behaviour. These particular data are from Survey 3 when the glitch rate was relatively constant and events above $10\sigma$ were selected to avoid any contamination by false events, solar flares, and pile-up. We cannot check multiple simultaneous events because we cannot distinguish between a pile-up of multiple events and a single more energetic event. Still, the glitch data are compatible with pure random events that are not correlated in time and this is consistent with the cause of events being individual hits by Galactic cosmic ray particles.

We also studied the coincidence of events between bolometers. We found that the largest fraction of coincidences, around 99%, are between PSB-a and PSB-b detector pairs in the same module (see below). The remaining roughly 1% of coincidences are particle shower events that effect a large fraction of the detectors in the focal plane in different modules (the shower events will be discussed in Sect. 5.7).

### 5.3. Interaction with the grid/thermistors

There is clear evidence that the short events result from cosmic rays hitting the grid or the thermistor. Indeed, these events have a fast rise time and have a fast decay, and the transfer function built from the short glitch template (see Catalano et al. 2014, for a comparison) is in good agreement with the HFI optical transfer function (Planck Collaboration VII 2014), so the energy must be deposited in the environment close to the thermistor. Figure 20 shows the cumulative counts, i.e., the number of events $N(>E)$ with an amplitude higher than a given value $E$ per hour, for short glitches, after converting the maximum amplitude of each glitch to units of energy (keV) for one reference bolometer (100-1b). The energy calibration for the other bolometers has been scaled so that the cumulative distributions match the one for the reference bolometer at energies of about 10 keV. For this conversion we use the measured heat capacity of the NTD crystal plus grid system (see Holmes et al. 2008), since we assume that the energy of the events is deposited in this system. The relative fitting of the energy is necessary for the comparison between bolometers
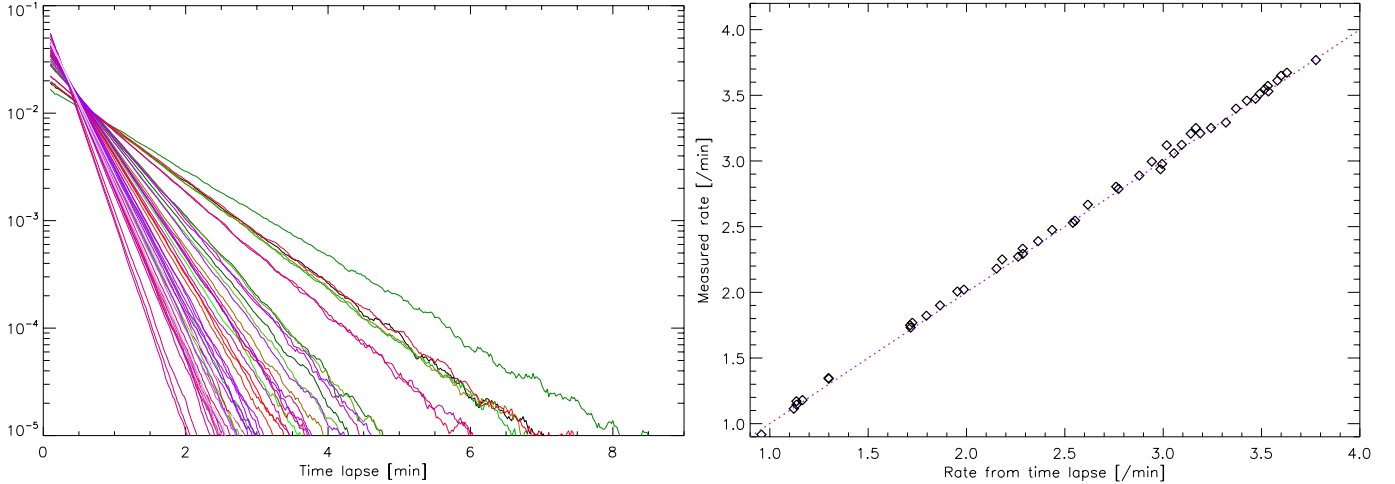
**Fig. 19.** *Left*: time interval between two consecutive glitch events for each bolometer, normalized by the total number of events. Colours distinguish different detectors. We observe Poisson distributions, as expected for random events. *Right*: glitch rate derived from the slope of the time interval distribution, compared to the mission averaged actual rate for each bolometer.
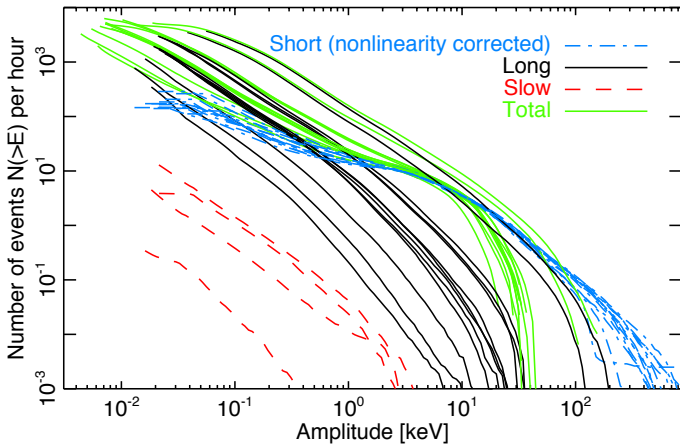


**Fig. 20.** Cumulative counts (per hour) for the three categories of glitches and for several bolometers: blue curves are for short glitches after non-linearity correction above typically 10 keV (as described in the text); black curves are for long glitches; red curves are for slow glitches; and green curves are for the total counts without the nonlinearity correction (which is why they lie below the blue curves). Glitches are not separated into the different categories below 10 times the rms noise (i.e., about 20 eV). All curves have been recalibrated in energy for each bolometer, such that the distributions of short glitches match at energies around 10 keV (we use the same coefficient for all populations), the absolute calibration being fixed for one arbitrary detector. Note that the distributions of short glitch match very well, while there is a large scatter in the energy scaling for the other populations of glitches.

because of uncertainties in the heat capacity of the system, and also in how much the peak amplitude is reduced after averaging over the interval of one sample within the electronics. Peak amplitude reduction is more important for faster bolometers. The effect is significant for the submillimetre channels, for which the time constant is very small. We determined that the relative correction factor should be about 3 for 100–545 GHz bolometers. We have also reconstructed and corrected the counts for high amplitudes that are affected by nonlinearity (typically above 10 keV) by readjusting the values of event energies using the measurements of the slow tails of short events (which are not affected by nonlinearity since they are too low in amplitude), instead of directly taking the peak amplitude. This allows us to

reconstruct the distribution more than a factor of ten above the saturation level set by the electronics. We can see in Fig. 20 that the counts of short events for all detectors match fairly well (considering the fact that no rescaling is performed on the $y$-axis, but only in energy), particularly around the energy bump.

Events in the bump are expected to be associated with cosmic rays hitting the thermistor. Since the thermistors are identical for all bolometers, we expect the same rates for all bolometers, which is precisely what we observe (Fig. 20). Given the dimensions of the thermistors of $30\,\mu$m $\times 144\,\mu$m $\times 341\,\mu$m, and the fact that typical Galactic protons of energies around 1 GeV (the peak of the spectrum) deposit minimum energies of $\approx 1.47\,$MeV cm$^2$ g$^{-1}$ in the Ge (which is the minimum of the stopping power for normal incidence in the largest surface), we expect typical deposition energies of 15 keV in the thermistor (the first energy being dominant, since it corresponds to the largest cross-section). This is also in agreement with the energy measured experimentally, given that the energy calibration is uncertain within about 50%. The amplitude of the bump in the cumulative distribution, which is at about 10 events per hour, also matches with the expectations. Indeed, by integrating the expected cosmic ray spectrum at L2, and considering that low energy particles are absorbed by the spacecraft, we can predict a total particle rate of $N \approx 5\,$s$^{-1}$ cm$^{-2}$. This leads to a glitch rate of about 8 h$^{-1}$ on the thermistor.

The events depositing an energy of about 10 eV to 1 keV and populating the power law seen in Fig. 20 are expected to be the result of cosmic rays hitting the grid. Calculations predict a total rate of events on the grid from 7 to 90 h$^{-1}$, given that the surface area of the grid varies from $4.77 \times 10^5\,\mu$m$^2$ to $3.95 \times 10^4\,\mu$m$^2$, depending on the bolometer. We observe a higher number of events, by a factor of 2–4, but (as we will see in the next paragraph) about half of the events for PSB bolometers might result from electrons ejected from the *other* grid by the impact of a cosmic ray proton. We observe some dispersion in the amplitudes of the power-law distributions from bolometer to bolometer, which is not obviously correlated with the area of the grids. This is attributed to the uncertainties in the intercalibration of energy to match the counts, as detailed at the beginning of this section.

We have performed a coincidence analysis of short events between PSB pairs. At the arrival time of each short glitch detected in a PSB-a bolometer, we have measured the level of
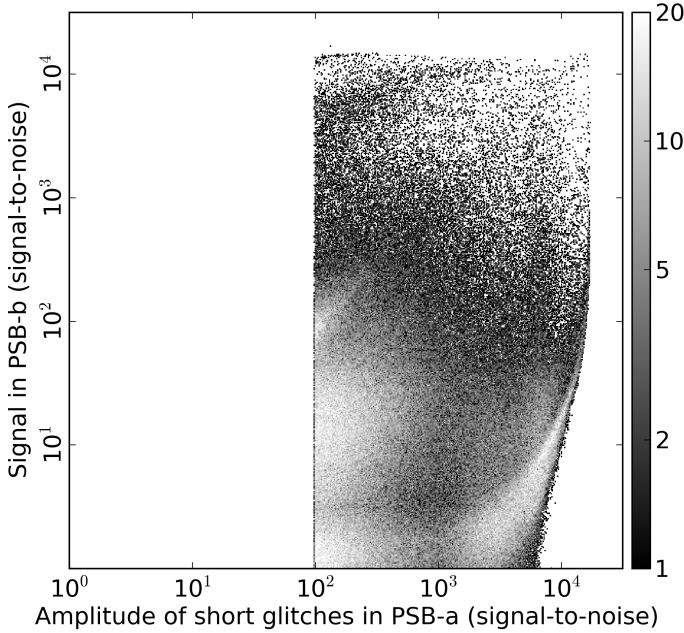
**Fig. 21.** Representative short glitch coincidences in a PSB pair. The *x*-axis represents the amplitude relative to the noise of the detected glitch in the PSB-a bolometer, while the *y*-axis is the value of the signal-to-noise ratio in the PSB-b bolometer. The grey-scale indicates the log of the number of events in logarithmic bins. Detected events are not shown below $100\sigma$ in PSB-a, as we expect a non-negligible contribution from long glitches, and the separation between long and short glitches is uncertain at low amplitudes. A large fraction of events are coincident between PSB-a and PSB-b.

signal in the PSB-b detector in the same module. We compare the amplitude of the signal in the PSB-b (without regard to the category of the signal in the PSB-b) with the amplitude of the glitch at its maximum in the PSB-a, and computed a 2D histogram of the two quantities. The 2D distribution of amplitudes for short glitches in the PSB-a is shown in Fig. 21. The events below $100\sigma$ are not displayed since the separation between short and long glitches is then uncertain. We observe that the distribution is very different from the expected distribution for random coincidence. The expected distribution of amplitudes for random coincidences is evaluated by measuring the statistics of the signal in the PSB-b at a time 10 000 samples (about one minute, i.e., well after a short glitch has terminated) after each event in the PSB-a, and this is shown in Fig. 22. In particular, we can see a wide cloud of points in the 2D histogram above about $10\sigma$ in PSB-b. A fraction of around 50% of the events populate the region of random coincidence. This is also shown in Fig. 23, which displays the distribution of the signal in the PSB-b for events in the PSB-a with amplitudes between 300 and $1000\sigma$. So there are strong indications that about 50% of short glitches are seen in coincidence between PSB-a and b. However, for a given amplitude of short glitch in PSB-a, we observe a wide distribution of amplitudes in PSB-b. We have verified that counterparts in PSB-b have no phase shift.

A possible model for these coincidences is that events hitting one of the grids eject some electrons which hit the other grid. The rate of 50% correlation can be explained by geometrical effects, such as particles coming from the top or bottom; a particle coming from the top could hit the PSB-a grid, extract electrons, and project those onto the PSB-b grid, whereas a particle coming from the bottom and hitting the PSB-a grid would not project electrons onto the PSB-b. The observations indicate,
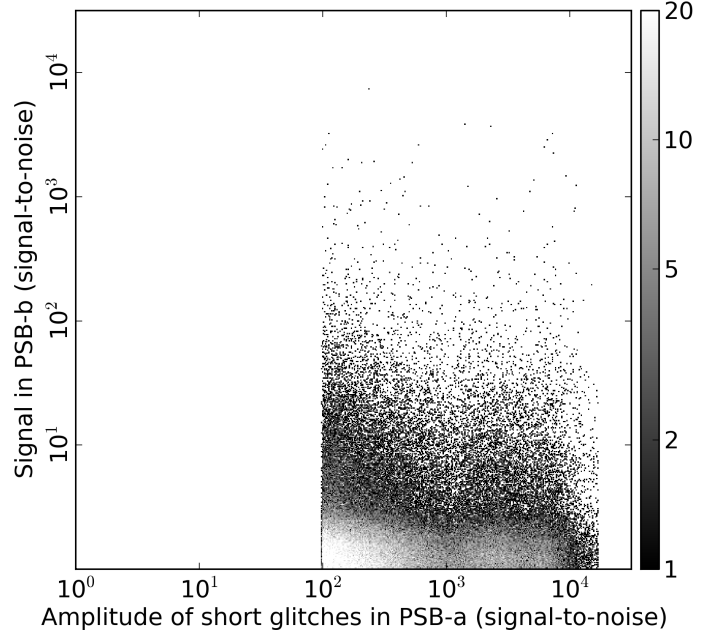


**Fig. 22.** Expected distribution for random coincidences, for comparison with Fig. 21. The value of the signal-to-noise ratio in PSB-b for each short event in PSB-a is taken 10 000 samples afterwards. We use short events in PSB-a so that this distribution can be directly compared to the coincidence of short glitches.
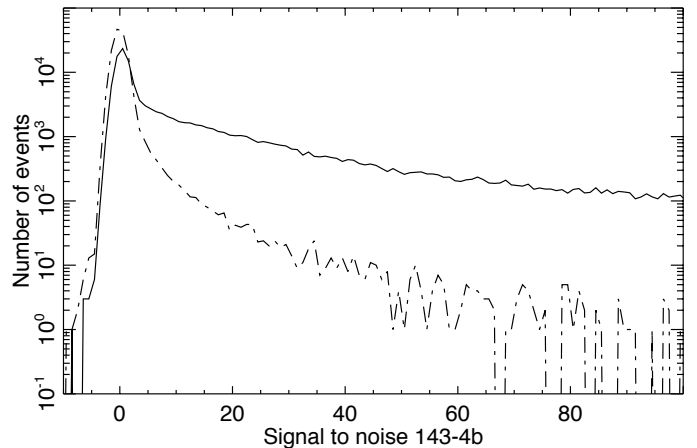


**Fig. 23.** Distributions of the signal values in PSB-b for short events with peak amplitudes between 300 and $1000\sigma$ in PSB-a (solid line). A random distribution of values in PSB-b is also shown (dot-dashed line). The excess of the solid curve over the dot-dashed curve for amplitudes above $3\sigma$ represents about 50% of the total area. Thus, at least 50% percent of the events are in coincidence between PSB-a and PSB-b.

then, that nearly all events hitting one of the grids and coming from the appropriate direction must eject electrons hitting the second grid and deposit about 10% of the energy deposited in the first grid. We also observe that some events clearly hit both grids. These appear in the cloud of points (in Fig. 21) with the same amplitude in both the PSB-a and b, representing about 2% of the events. We observe a lower coincidence rate for events at higher amplitudes corresponding to the bump. This is explained by the hypothesis that those events correspond to direct impacts on the thermistor, which is not aligned with the grid of the other bolometer. Nevertheless, we have seen that all those high energy events are in coincidence with a small amplitude event in the second bolometer. This is attributed to the cross-talk

between bolometers in a pair, as discussed in Sect. 5.5. The non-linearity, appearing as the curved shape in the coincidences, can be entirely explained by the saturation of the highest amplitude glitches. Nevertheless, we can evaluate the level of cross-talk to be between 0.01 and 0.44%, depending on the bolometer pair, for about $3000\sigma$ events (for which the effect of saturation is small). The high amplitude events correspond to an energy of $\approx 15$ keV left on the grid+thermistor by a particle; this is very close to the expected energy deposited by a 1 GeV proton onto the thermistor.

## 5.4. Interaction with the wafer

We identify the long glitches as being produced by cosmic rays hitting the silicon die. This was first indicated by the ground tests (Catalano et al. 2014), showing that the NTD thermometer is sensitive to a temperature change of the Si die. The HFI ground-based calibration data show a rate of events compatible with the cosmic ray flux at sea level over the Si die surface, and the ground-based data also show that almost all these events are in coincidence between PSB-a and PSB-b. Our understanding is the following. Hot carriers are generated by the particle impacts on the Si die. These rapidly decay into hot ballistic phonons which cause the rapid (athermal) rise in NTD Ge temperature. The bolometer temperature then decays with fast optical time constant. The next slower time constant is due to the thermal response of the Si die (Catalano et al. 2014). The slowest thermal response is due to the heat flow through the copper module and into the 100 mK heat sink (Spencer et al., in prep.) This hypothesis is reinforced by the comparison of cumulative counts $N(>E)$ of long glitches from bolometer to bolometer (Fig. 24). To make this comparison, we have normalized the counts so that we are evaluating the number of events per unit time and per unit surface area of the Si wafer (because the total surface varies from bolometer to bolometer). Also, as for short glitches, we have intercalibrated the energies of events between bolometers by matching the different counts at measured energies around 0.05 keV, which corresponds to a deposited energy on the Si die of about $10^3$ keV after absolute calibration. This absolute calibration is performed so that the observed faint-end break of the counts, which is clearly visible in the figure, matches the expected minimum energy deposited by GeV protons on the Si die (which is about 140 keV, for normal incidence, as described later). This calibration of the model is necessary, since we only measure the energy in the grid+thermistor system, and the heat capacity and link conductivities are not known with sufficient accuracy. Additionally, we use the values of the peaks to record the amplitudes of glitches that are not representative of thermal processes, since the fast part of long glitches is expected to result from ballistic phonon effects.

Figure 24 shows the cumulative counts for all the HFI bolometers used for the scientific analysis. We clearly see that they all match in shape and amplitude, with very small scatter. For energies below 20 times the rms noise, we have also computed the cumulative counts for all events, without distinction between families (green curves in the figure); we have already seen that long events dominate at low energy, so the total counts are representative of the counts of long glitches. The faint-end break in the counts is detected without ambiguity. This is an important result, since it shows that there are a limited number of undetected low energy glitches in data, which might otherwise affect the cosmological results. From this limit, we measure that the total rate of events penetrating the shielding of the satellite around the bolometers is about $4.5\,\mathrm{s}^{-1}\,\mathrm{cm}^{-2}$. This is in
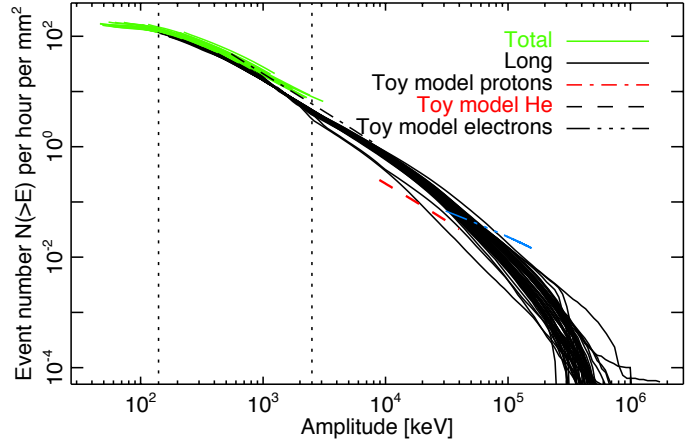


**Fig. 24.** Cumulative distribution $N(>E)$ of long glitches per unit surface area of the wafer for all bolometers used for the scientific analysis. The black solid lines correspond to selected long glitches. The green lines correspond to total glitches, but are representative of long glitches, since they dominate at low energy. We have used a relative calibration of the energy (indicated on the $x$-axis) such that the cumulative counts for all bolometers match at $10^3$ keV. The absolute calibration of the energy is set so that the faint-end break of the counts matches the expected deposited energy of about 140 keV in the Si die. Nevertheless, we observe that the shape of the cumulative counts match for all detectors, and with a low dispersion. The break in the counts at the faint end is very significantly detected; this is our best indication from flight data that long glitches result from particles hitting the Si die of the bolometer. Dot-dashed and dashed lines correspond to the predicted power-law distributions of deposited energy from protons and helium, respectively, with a toy model for the interaction on the wafer using the incident particle spectrum at L2 for energies significantly higher than the stopping power energies. Predicted minimum deposited energies for He and for protons are indicated with dotted lines. We interpret the second apparent bump (seen as a slight break in the spectrum at around 20 times the energy of the main break) as the signature of He nuclei.

good agreement with the expected value in the bolometer environment computed in Sect. 5.3 of $5\,\mathrm{s}^{-1}\,\mathrm{cm}^{-2}$. The slope and amplitude of the distribution can be predicted using a simple power-law model of the interaction of primary Galactic protons and He nuclei with the Si die, as shown in Fig. 24. We observe a good match of the model with the data, showing that particles detected by *Planck* at the energies above the faint-end break are primary Galactic protons. The barely apparent second bump in cumulative counts at deposited energies around 3000 keV may correspond to the contribution from He nuclei, which are expected to contribute about 10% of the counts at those energies. The fact that we observe an excess in the counts at the expected energy of the minimum stopping power for He reinforces our hypothesis for the origin of long glitches. High energy Galactic electrons could also contribute to the measured counts for high deposited energies.

The large scatter in the distributions of long glitches with respect to different detectors, after calibrating the energy on the short distributions, is shown in Fig. 20. This is due to the variation of thermal links between the grid and the Si die, as well as variations in the Si die heat capacity, reducing or increasing the fraction of energy transmitted to the thermistor for both phonons and thermal processes. The detectors with smaller glitch counts (e.g., 143-1a and 143-5 in Fig. 17) are those with a smaller fraction of the energy propagating from the wafer to the grid. For those detectors we do not see the break in the counts, since it should be below the detection threshold. We observe that in
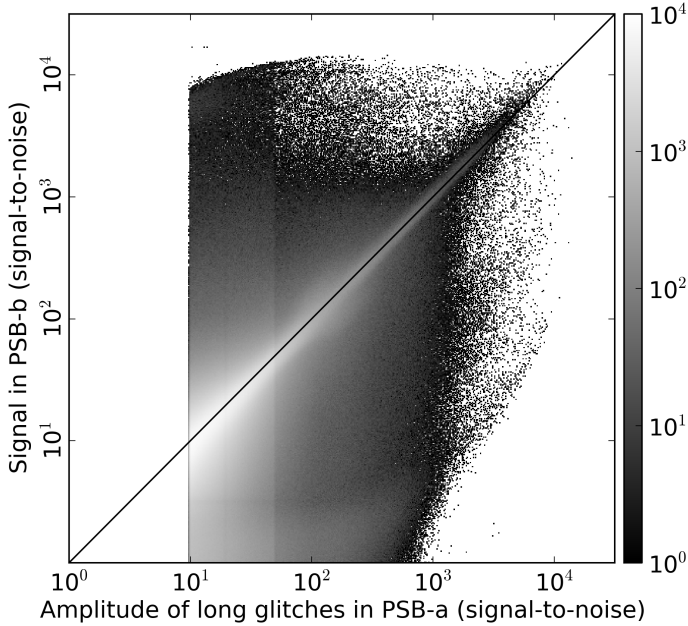
**Fig. 25.** Representative long glitch coincidences in a PSB pair. See description in Fig. 21. Events above $50\sigma$ are selected if they match the long glitch template. All events (without selections) are included below $50\sigma$, since the long glitch population dominates at low amplitudes. The solid line indicates identical signal in both the PSB-a and PSB-b. Most (if not all) long events in PSB-a are associated with significant events in PSB-b, and a large fraction have approximately the same amplitude in PSB-a and PSB-b.
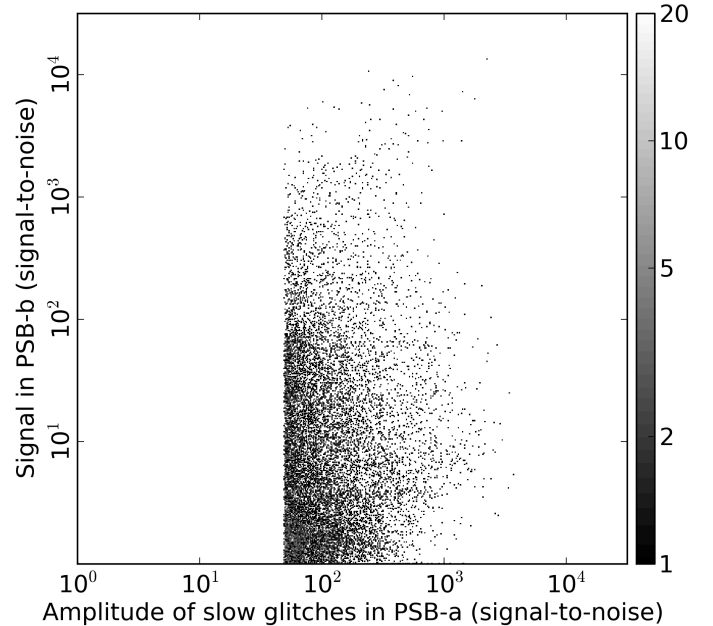


**Fig. 26.** Representative slow glitch coincidences in a PSB pair. See description in Fig. 21. No event is shown below $50\sigma$, to avoid leakage from the long population. All slow glitches in PSB-a above about $1000\sigma$ are associated with significant events in PSB-b. Below about $1000\sigma$ the majority of events are associated with significant events in PSB-b. For the remaining fraction the fact that we do not see a significant signal might be simply a threshold effect.

general PSB-b detectors are more sensitive to long glitches than PSB-a detectors (although a few exceptions exist).

Detectors with smaller rates of glitches should have more undetected glitches than detectors with a higher rate. This hypothesis is verified with the help of the cross-correlation analysis between bolometer signals from the same PSB pair, described in Sect. 3.2 (see Fig. 13 in particular). We observed that bolometer pairs with smaller glitch rates are those with higher correlations around 1 Hz, which is attributed to glitches below the threshold. On the other hand, pairs for which one of the bolometer has a visible faint-end break in the counts have smaller correlations in the noise. The impact of this on final results after processing is studied in Sect. 4.2.

We have already seen that events hitting the bolometer Si die must deposit a fraction of their energy, which is typically the minimum stopping power of the Si for events close to normal incidence and with energies of 140 keV. Then, most of the events must instantaneously hit the two wafers in PSB pairs. This is compatible with what we observe by measuring the coincidence of long events in PSB-a with signal in PSB-b, shown in Fig. 25, as we did for short events. Indeed, we find that between a third and a half of the events deposit the same energy in both PSB-a and PSB-b detectors, with some intrinsic dispersion, as most of the points lie along a line in the figure. The factor between amplitudes of coincident events is almost 1 in signal-to-noise units for this PSB pair, but can vary between 0.25 and 4, depending on the bolometer pair. This factor becomes 1 after recalibrating in units of deposition energy on the Si die, as expected. Furthermore, 100% of the events (at least for amplitudes higher that $300\sigma$) happen in coincidence between the two bolometer pairs, but with different energy deposition, by a factor of 300 at maximum. We cannot state this for events below $300\sigma$, since a significant fraction of the counterparts in PSB-b are below the noise level. We

could explain the difference in energy deposition between PSB-a and PSB-b by the fact that some relatively low energy events lose a significant fraction of their energy in the first Si die and then deposit more in the second, since the stopping power is a decreasing function of the energy for the considered particles. Some electrons could also be ejected from the first wafer and interact with the second wafer (as discussed for the grid interaction), but the associated signal would be diluted in the signal from the primary particle, since the events are in coincidence in the two wafers. In principle we should have a small proportion of events hitting the corner of the bolometer wafer, with no counterparts in other bolometers, but we do not have evidence for such events. The number of events in the distribution along the line of one-to-one correlation is of the order of 50% of the total number for events with amplitudes lower than about $300\sigma$ or above about $1500\sigma$, and is around 35% for amplitudes in between. A complete modelling of the interaction of particles with the two Si dies, including accurate physical modelling of the interaction, is postponed to a forthcoming publication.

Crucially, the coincidence study indicates that the contribution to the glitches by secondary particles, e.g., "delta" (or secondary) electrons, is negligible, since those low energy events would deposit all their energy in the first wafer without a counterpart in the second.

We have also performed a coincidence analysis at the location of slow events in PSB-a. Distributions are shown in Fig. 26. As already stated, slow glitches are seen only in PSB-a. Nevertheless, there is a significant signal in PSB-b associated with slow glitches in PSB-a. Indeed, we can see that the distribution of counterparts in PSB-b is very different from the random distribution shown in Fig. 22, which means that slow events in PSB-a are associated with signals in PSB-b. The counterparts generally have a wide range of amplitudes for a given energy

of slow glitches, which makes it difficult to measure the associated time constants. Visual inspection of those events allows us to distinguish a variety of counterparts: some have faster decay than slow glitches and have similar rise times of around 10 ms; and some others (the larger energy ones) are similar to long glitches.

### 5.5. Cross-talk between bolometers

A very high amplitude short event in one of the bolometers of a PSB pair is always seen in coincidence with a small event in the other bolometer. This is attributed to cross-talk between bolometers. The estimated level is about $10^{-3}$, as can be seen in Fig. 21 for a particular pair; the level varies between 0.01 and 0.44% for different pairs. These events show a phase shift, which varies from 0.25 to 1.4 samples, depending on the pair, and the transfer function of the cross-talk signal is different from the primary glitch transfer function. We observe longer time constants for the cross-talk signal than for the bolometers, ranging from 10 to 30 ms. The origin of cross-talk between detectors from the same PSB pair might be electrical or thermal; there is no clear evidence at this point.

We have also attempted to estimate the cross-talk signal between bolometers which are not mounted in the same pair. To do so we have averaged the bolometer signal at locations of detected high energy events in one of the bolometers. We found a significant (but very small) cross-talk signal of the order of $3 \times 10^{-5}$ for some pairs of detectors within the same electronics belt. However, we did not measure any significant signals in data from other bolometers, with an estimated limit of $3 \times 10^{-6}$.

### 5.6. Solar flares

For most of the mission, solar activity was remarkably low (Mewaldt et al. 2010). In 2011, for the first time in the mission, there were several large solar flares. These flares provided useful test cases for correlating the signal measured on the outside of the spacecraft (with the SREM) with signals due to particle impacts on HFI. The glitch rate noticeably increases during solar flares. The heater power used to regulate the 0.1 K plate decreases with increasing signal, and hence the particle flux, measured by the SREM diode sensors (Fig. 27). The timescale of each flare was slow enough that the temperature control loop was able to compensate for the bulk heating produced by the increased particle flux, as shown by the small phase shift of the heater power compared to the onset of the signal in the SREM. We see in Fig. 27 that the peak measured signal for TC1 and TC3 differ by only about 40% for the two flares. The signals of the heater power and TC2 are similar to each other in each flare. However, the peak signal of each is very different when comparing the two flares. In addition, there is structure in the signal for TC1 and TC3, which is not seen in TC2 or the heater power response. We find that this correlation holds between the heater power and TC2 for all flares. The diode TC2 has the most shielding of the three diodes in the SREM, 1.7 mm of aluminium and 0.7 mm of tantalum, which passes only ions and protons with energies >39 MeV. The other diodes are shielded by 0.7 mm of Al for TC3 and 1.7 mm of Al for TC1. This demonstrates that the spacecraft and the instrument surrounding the bolometers act to shield particles with energies at least up to 39 MeV, as well as all solar electrons. This is similar to the stopping power of about 1.5 cm of Al[3].

---

[3] http://physics.nist.gov/Star
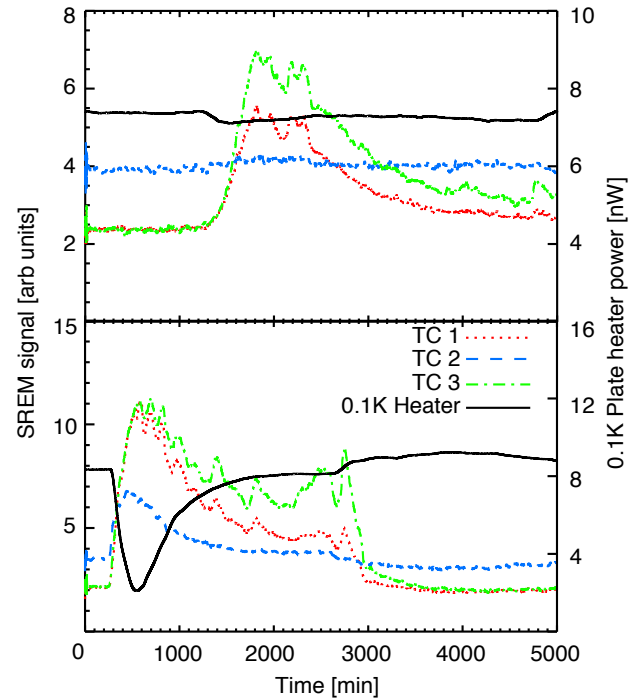
**Fig. 27.** Output of SREM diodes TC1, TC2 and TC3 (*left axis*) and temperature control heater power on the 0.1 K plate (*right axis*), and as a function of time for large solar flares on 7 March 2011 (*top*) and 4 August 2011 (*bottom*).

### 5.7. High coincidence events

Since the beginning of the *Planck* mission, large temperature increases of the 0.1 K plate have been observed through the bolometers and thermometers. These events have two specific characteristics. There are a high number of glitches detected at the same time in multiple bolometers, and there is an increase of the focal plane temperature in the range of nanokelvins to microkelvins. In this section we will analyse the characteristics of these high coincidence events (HCEs).

#### 5.7.1. Detection

HCEs are identified by detecting a large number of precursor glitches in coincidence in different detectors (so called "touched" bolometers) on the 0.1 K plate. These coincidences happen before a temperature excursion of the 0.1 K plate. Other automated techniques that focus on finding only the temperature excursion were applied to the data, but were not successful at identifying HCEs in the time stream. One reason for this is that for most of the events this temperature rise is below the thermometry noise level.

Figure 28 shows the histogram of the number of events in coincidence for the full mission for 15 ms bins. The distribution at low number of coincidences is nearly compatible with random coincidence, given the measured rate of glitches per bolometer. The distribution deviates from random coincidences above 13 "touched" bolometers. We set the detection threshold at 15 in order to select only real coincidences linked with HCEs. We detect around 100 000 HCEs for a theshold of 15, or an average of 5 events per hour.
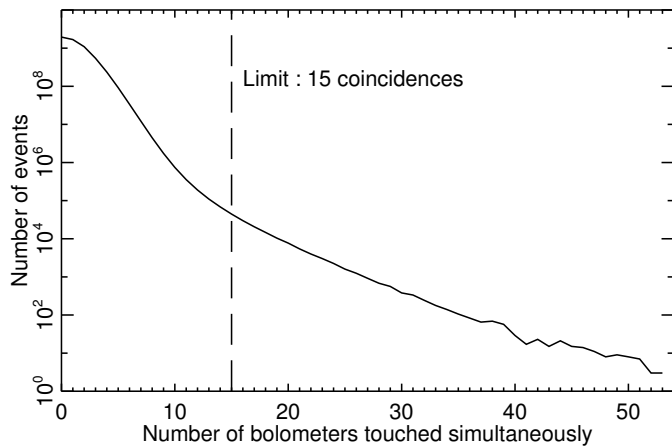
**Fig. 28.** Coincidence histogram (solid line) processed for the entire mission, based on the result of the glitch detection algorithm. Random coincidences dominate for low numbers of "touched" bolometers. Coincidences above 15 bolometers are real correlations (dashed line).

### 5.7.2. Different types of HCE

For each event above the thermometry noise level we calculate separately the median of the temperature time stream for "touched" bolometers and for bolometers without a precursor glitch, or "untouched" bolometers. We can separate events into two categories, fast and slow, which differ in the rise time of the temperature (Fig. 29). The maximum temperature value is calculated in the range 8–12 s after concidence for fast events, or 80–120 s after the coincidence for slow events.

For fast HCEs, coincident glitches occur in several (but not all) bolometers, and are grouped together on the 0.1 K plate. The temperature rise time constant is around 5 s. The decay time constant is approximately 20 min and matches the thermal time constant of the 0.1 K plate.

The precursor glitches for a fast HCE are short or long glitches. The separated "touched" and "untouched" bolometer temperature time stream stacking averages, for fast HCEs greater than $1.5\,\mu$K, are shown in Fig. 29. The "untouched" curve rises slowly, but decays in phase with the "touched" one after all bolometers thermalize with the entire 0.1 K plate. The distribution of fitted temperature amplitudes for all the fast HCEs (coincidence of greater than 15 bolometers) obtained by template fitting is given in the left panel of Fig. 30. We observe that fast events above $0.8\,\mu$K are individually detected. For events detected with signal-to-noise ratio less than one, we find a non-zero amplitude of $0.057\,\mu$K. We also observed that the rate of fast HCEs is modulated in the same way as cosmic rays over the mission.

The fact that the "touched" bolometers are grouped in the focal plane and precursor glitches of fast HCEs are the same as for individual particle hits directly on the Si die (for long glitches) or grid (for short glitches), leads us to conclude that these events are due to showers of secondary particles over part of the focal plane. The temperature increase of the 0.1 K plate results from the low energy secondary particles from the shower, which are stopped by the bolometer plate. The rate of the most energetic events is consistent with the geometry of the 0.1 K plate and the flux of Galactic cosmic rays that are energetic enough ($\gg$GeV) to produce such showers (Adriana 2011).

For slow HCEs, the coincident precursor glitches occur in all, or nearly all, bolometers. As shown in Fig. 29, there is a small temperature decrease around 1 s after the precursor

glitch and before the temperature rise, with a time constant of about 30 s and, as observed for fast HCEs, a decay time constant of about 20 min. This initial decrease prior to the rise is not yet understood.

The precursor glitches for these HCEs are very specific and seem to be different from any of the categories studied in Sect. 5. They have a rise time of about 10 ms and a decay time that varies from event to event, but is of order 100 ms, which is a lower value than for the slow glitches (see Sect. 2.3). The distribution of fitted temperature amplitudes for all the slow HCEs is shown in Fig. 30 (right panel) and the validation threshold value is 1.3 $\mu$K. Slow HCEs have a less steep distribution than fast HCEs, and dominate above 2 $\mu$K. In contrast to fast HCEs, we have observed that the rate of slow events decreases through the mission. We use the measured thermal properties of the 0.1 K plate (Planck Collaboration II 2011) to estimate that slow HCEs correspond to an energy deposition of around 1 TeV, with a rate that is not consistent with the Galactic cosmic ray spectrum (Adriana 2011). We have also considered elastic relaxation of cracks and anomalous response of the 0.1 K stage PID loop as possible explanations. However, we have yet to reproduce a slow HCE experimentally on the flight focal plane, for example with temperature or heater steps, or in analogous ground tests. At this time, we have not identified a physical cause for the slow HCE events.

### 5.8. Particle interaction with bolometer plate

It has been shown in Planck Collaboration II (2011) that interactions of particles with the bolometer plate are responsible for the correlated low frequency noise between bolometers (see Fig. 13 and caption). This excess noise was not seen in ground measurements (Pajot et al. 2010) and is modulated with solar activity in the same way as the glitch rates.

Although the mean temperatures of the 0.1 K and dilution cooler plates are stabilized with great precision, this is only at a single point near the control heater. Distributed heating from particles and other sources causes gradients within the plate. As described in Planck HFI Core Team (2011b), the signal from the two dark bolometers was used to track the temperature of the 0.1 K plate, independent of the control thermometer. NTD thermometers could not be used to control the temperature variations because of the very high glitch rates due to their large volume. The signal from each dark bolometer was smoothed over a running window of 2 min (or about two full rotations of the spacecraft) and combined to form a thermal template, which was then cross-correlated with each bolometer and used to remove long-term drifts from the bolometer time streams. Both the control heater power and the thermal templates are correlated with diode sensors in the SREM, indicating that a significant source of heating (although small, <10 nW) comes from interaction with the particle flux.

We have evaluated the contribution of fast HCEs to the bolometer noise power spectrum. We start by assuming that the distribution of the amplitudes of fast events follows the fitted power law shown in Fig. 30. Since the power law has a high index (around 3), some break has to occur towards the lowest amplitudes. By choosing a limit about 10 times lower than the amplitude corresponding to where the total counts match the detected number of coincidences for 15 "touched" bolometers, we found that fast HCEs might account for approximately 10% of the correlated low frequency noise between bolometers. By selecting events above 15 coincidences only, we are not counting all actual coincidences, since coincidence of a
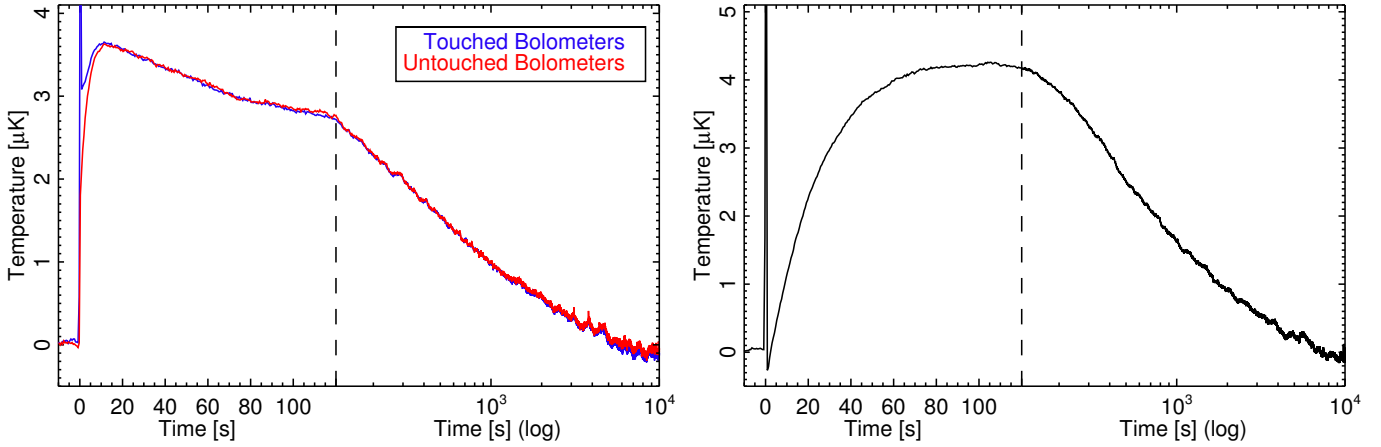
**Fig. 29.** Stacking of 69 fast HCEs for bolometers detected as "touched" and "untouched" and 72 slow HCEs for all bolometers. The scale changes from linear to logarithmic at 100 s. For fast HCEs (*left panel*), the limit is clear, and the stacking of "untouched" bolometers gives the thermal time constant of the copper/stainless steel bolometer plate heating. For slow HCEs (*right panel*) we observe a temperature decrement lower than 1 $\mu$K for about 1 s before the temperature rises, and this is not understood.
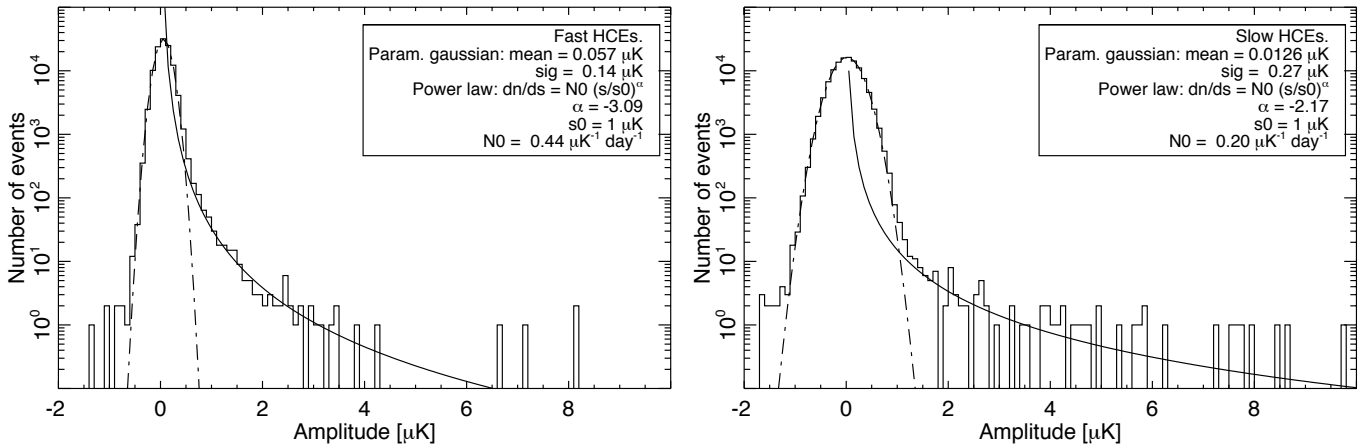


**Fig. 30.** Amplitudes of fast (*left panel*) and slow (*right panel)* HCEs. Amplitudes are computed by jointly fitting fast and slow templates. Solid lines correspond to power laws fitted to the tails of distributions (above 1 $\mu$K), the high amplitude fast events above 7 $\mu$K being removed from the fit; the number of those high amplitude fast events is not compatible with the power-law distribution. Dot-dashed lines are Gaussians fit to the distributions near zero amplitude and are representative of fitting errors. Parameters of the fitted distributions are given in the figure legend. Fast events (and to some extent slow HCEs) have a varying temporal shape from event to event. It appears that the variation can be fit by a contribution from the slow HCE template. This explains in part the negative tail of the distributions of fitted amplitudes. The rest may be confusion between events inducing an anti-correlation of amplitude parameters.

few bolometers ($<10$) are overwhelmed by the random events. We have tried techniques such as fitting HCE templates over a sliding window in the temperature of the 0.1 K plate (measured by the thermal template), but have not found one that successfully detects the bulk thermal response of the 0.1 K plate from fast HCEs without the precursor coincidence flagging. However, even a modest increase in the total HCE events with $<10$ bolometers in coincidence could explain all of the correlated noise. We are pursuing models and analysis techniques to quantify more accurately the number and effect of these undetected coincidences.

### 5.9. Other events

The origin of slow glitches is not entirely understood. Laboratory tests using alpha particles were unsuccessful at reproducing slow glitches. Nevertheless, the similarities with long glitches suggest that both populations have the same physical origin, and that they correspond to some energy injected into the wafer. A key feature of the slow glitches is that they only occur in the PSB-a detectors. The mechanical mounting of the PSB-a bolometers is different from that of the PSB-b and the SWB bolometers. Tests using heaters and thermometers mounted at different locations near the PSB-a are in progress, to attempt to identify any unique thermal feature that could cause a slow glitch.

One of the bolometers (100-1a) shows another category of glitch that is not detected in any other bolometer. These particular events have a slow response, which is similar to the slow tail of short glitches, but do not show a fast decaying part. They also have a rise time constant of around 10 ms. Such events are not accounted for in our glitch subtraction method and this induces a small excess in the residual power spectra at frequencies around 0.1 Hz (see Fig. 12, and Sect. 3.2 for a discussion of the impact of such events). This excess is accounted for in the total noise budget for cosmological studies (Planck Collaboration XV 2014).

Finally, precursors of slow HCEs are events that are only seen in coincidence and when associated with slow HCEs (see Sect. 5.7 for a description). They are not accounted for by the

glitch subtraction method, but are rare enough that they do not affect the cosmological data analysis.

## 6. Conclusions

In this paper we have proposed an interpretation of the source of the glitch signals observed in *Planck*-HFI bolometer data, we have presented details of our glitch subtraction and flagging method, and we have evaluated the impact of residual glitches on cosmological data after processing.

We observed three families of glitches, "short", "long", and "slow", where each is described by a sum of three or four exponentials. They can be distinguished from each other by the relative amplitudes and time constants of these exponential terms. The rate of each glitch type is anticorrelated with solar activity, indicating that they are all due to energy deposition by Galactic cosmic rays. Using the response of the on-board particle monitor and cryogenic stages during solar flares, we find that the spacecraft and surrounding instrument mass shields the 0.1 K plate and bolometers from all particles with energies less than 39 MeV.

Short glitches have a response similar to the optical response of the bolometers. These short glitches result from direct particle energy deposition in the grid, for the lowest energies, or in the Ge thermistor for the highest energies.

Long glitches dominate the total glitch count rate, but are usually smaller in amplitude than the short glitches. Long glitches show a fast part with about a 10 ms time constant, followed by the sum of slow exponentials, with around 50 ms to 2 s time constants. We find that the flux of the long glitches is the same for all bolometers, when we scale with the area of the Si die. Coincident counts in the PSBs paired in a single bolometer module in the flight data, as well as laboratory tests of spare bolometers on the ground using alpha sources to expose the absorber grid and Si die separately, and tests using a 23 MeV proton beam line, support the conclusion that long glitches are due to particles depositing energy in the Si die. We find a minimum energy deposition in the count distribution of long glitches that corresponds to a proton with an energy at the minimum of the proton energy loss spectrum traversing the Si die normal to the surface. This minimum deposited energy is above the noise threshold for about half of the detectors. Thus we can individually detect almost all of the glitches in the bolometer data. We suspect that the fast part is due to hot ballistic carriers propagating from the wafer to the thermistor. The slower timescale response is from the thermal relaxation of the Si wafer. We find evidence of long glitches caused by Galactic cosmic ray He, but no evidence of Galactic cosmic ray electrons. Low energy showers of secondary or delta electrons were earlier suspected to be the cause of the high rate of glitches in HFI. However, the high rate in PSBs is measured in coincidence between the two bolometers. This signature cannot be caused by a delta electron shower. On the other hand, there is evidence of delta electrons in the coincidence of short glitches in PSB pairs. In this process, the delta electrons are produced when a high energy particle hits the absorber grid of one bolometer and produces a coincident glitch at high probability and at lower energy, in the neighbouring grid.

Slow glitches are not understood at this time and have not been replicated in the laboratory. These glitches have nearly the same long timescale behaviour as long glitches and are thus expected to be due to energy deposition somewhere else in the module.

We detect high energy secondary showers from very high energy events, both through coincident glitch detection among

many bolometers and in heating of the 0.1 K plate. The rate (about $5 \, h^{-1}$) and energy of these events is consistent with the impact of Galactic cosmic rays at very high energies, >1 GeV per nucleon.

We also detect a second type of high energy event with a different time response than that of the secondary showers. These have a characteristic energy of around a TeV and a rate that is too high to be due to cosmic rays. We currently do not have an explanation for the cause of these events.

The new glitch analysis presented here is a considerable improvement over the one previously reported. The method iterates between sky signal estimated ring by ring independently, and glitch detection above 3.2 times the rms noise after subtraction. The sky signal is carefully estimated before subtraction using spline interpolation to avoid spurious event detection. For a better separation of glitches into different categories, we employ for each detected event a joint fitting of the three glitch types, using templates. Long and slow glitch templates are subtracted from the data. Without this subtraction, residual glitch tails, after flagging would dominate over the noise for a large range of timescales. The glitch removal method improves the noise performance of HFI; we found that the residual contribution from glitches after template subtraction is below the noise at all frequencies, and has a maximum amplitude at around 0.1 Hz. Realistic simulations, including the modelling of glitches, support this result, and show for the two bolometers studied at 143 GHz that residual glitches contribute to less than 20% of the noise spectrum on scales (along the scan) larger than about 2°. At smaller scales the residual contribution is smaller than 5% and is induced by long glitches below the threshold. This conclusion is supported by the observed correlations between the signals from bolometers in a PSB pair.

The rapid part of all detected events is flagged. Consequently, the amount of data rejected from the astrophysical analysis varies from 8% to 20%, depending on the bolometer. This should be contrasted with the >95% of acquired samples that are affected by glitches in the unprocessed data.

With the help of the simulations, we have evaluated potential biases introduced by our method on the sky signal estimation. We find no evidence of bias in the cosmological signal and we estimate an upper limit of $10^{-4}$ on the CMB anisotropy power spectrum.

## References

Adriana, O. E., Barbarino, G. C., Bazilevskaya, G. A., et al. 2011, Science, 332, 69
Benoît, A., Ade, P., Amblard, A., et al. 2003, A&A, 399, L19
Bobik, P., Boella, G., Boschini, M., et al. 2012, ApJ, 745, 1
Bock, J. J., Chen, D., Mauskopf, P. D., & Lange, A. E. 1995, Space Sci. Rev., 74, 229
Catalano, A., Ade, P., Atik, Y., et al. 2014, A&A, 569, A88
Crill, B. P., Ade, P. A. R., Artusa, D. R., et al. 2003, ApJS, 148, 527

Delabrouille, J., Betoule, M., Melin, J.-B., et al. 2013, A&A, 553, A96
Gleeson, L. & Axford, W. 1968, ApJ, 154, 1011
Griffin, M. J., Abergel, A., Abreu, A., et al. 2010, A&A, 518, L3
Holmes, W. A., Bock, J. J., Crill, B. P., et al. 2008, Appl. Opt., 47, 5996
Jarosik, N., Barnes, C., Greason, M. R., et al. 2007, ApJS, 170, 263
Jones, W. C., Montroy, T. E., Crill, B. P., et al. 2007, A&A, 470, 771
Lamarre, J., Puget, J., Ade, P. A. R., et al. 2010, A&A, 520, A9
Maffei, B., Noviello, F., Murphy, J. A., et al. 2010, A&A, 520, A12
Masi, S., Ade, P. A. R., Bock, J. J., et al. 2006, A&A, 458, 687
Mewaldt, R., Davis, A., Lave, R., et al. 2010, ApJ, 723, L1
Mohammadzadeh, A., Evans, H., Nieminen, P., Daly, E., et al. 2003, IEEE Trans. Nucl. Sci., 50, 2272
Pajot, F., Ade, P. A. R., Beney, J., et al. 2010, A&A, 520, A10
Patanchon, G., Ade, P. A. R., Bock, J. J., et al. 2008, ApJ, 681, 708
Planck Collaboration I. 2011, A&A, 536, A1
Planck Collaboration II. 2011, A&A, 536, A2
Planck Collaboration I. 2014, A&A, 571, A1
Planck Collaboration II. 2014, A&A, 571, A2
Planck Collaboration III. 2014, A&A, 571, A3
Planck Collaboration IV. 2014, A&A, 571, A4
Planck Collaboration V. 2014, A&A, 571, A5
Planck Collaboration VI. 2014, A&A, 571, A6
Planck Collaboration VII. 2014, A&A, 571, A7
Planck Collaboration VIII. 2014, A&A, 571, A8
Planck Collaboration IX. 2014, A&A, 571, A9
Planck Collaboration X. 2014, A&A, 571, A10
Planck Collaboration XI. 2014, A&A, 571, A11
Planck Collaboration XII. 2014, A&A, 571, A12
Planck Collaboration XIII. 2014, A&A, 571, A13
Planck Collaboration XIV. 2014, A&A, 571, A14
Planck Collaboration XV. 2014, A&A, 571, A15
Planck Collaboration XVI. 2014, A&A, 571, A16
Planck Collaboration XVII. 2014, A&A, 571, A17
Planck Collaboration XVIII. 2014, A&A, 571, A18
Planck Collaboration XIX. 2014, A&A, 571, A19
Planck Collaboration XX. 2014, A&A, 571, A20
Planck Collaboration XXI. 2014, A&A, 571, A21
Planck Collaboration XXII. 2014, A&A, 571, A22
Planck Collaboration XXIII. 2014, A&A, 571, A23
Planck Collaboration XXIV. 2014, A&A, 571, A24
Planck Collaboration XXV. 2014, A&A, 571, A25
Planck Collaboration XXVI. 2014, A&A, 571, A26
Planck Collaboration XXVII. 2014, A&A, 571, A27
Planck Collaboration XXVIII. 2014, A&A, 571, A28
Planck Collaboration XXIX. 2014, A&A, 571, A29
Planck Collaboration XXX. 2014, A&A, 571, A30
Planck Collaboration XXXI. 2014, A&A, 571, A31
Planck HFI Core Team 2011a, A&A, 536, A4
Planck HFI Core Team 2011b, A&A, 536, A6
Reinecke, M., Dolag, K., Hell, R., Bartelmann, M., & Enßlin, T. A. 2006, A&A, 445, 373
Usokin, I., Bazilevskaya, G., & Kovaltsov, G. 2011, J. Geophys. R., 116, 1
Wiedenbeck, M., Davis, A., Leske, R., et al. 2005, in 29th International Cosmic Ray Conference Pune, 101

[1] APC, AstroParticule et Cosmologie, Université Paris Diderot, CNRS/IN2P3, CEA/lrfu, Observatoire de Paris, Sorbonne Paris Cité, 10 rue Alice Domon et Léonie Duquet, 75205 Paris Cedex 13, France

[2] Aalto University Metsähovi Radio Observatory, Metsähovintie 114, 02540 Kylmälä, Finland

[3] African Institute for Mathematical Sciences, 6-8 Melrose Road, Muizenberg, 7945 Cape Town, South Africa

[4] Agenzia Spaziale Italiana Science Data Center, via del Politecnico snc, 00133 Roma, Italy

[5] Agenzia Spaziale Italiana, Viale Liegi 26, Roma, Italy

[6] Astrophysics Group, Cavendish Laboratory, University of Cambridge, J J Thomson Avenue, Cambridge CB3 0HE, UK

[7] Astrophysics & Cosmology Research Unit, School of Mathematics, Statistics & Computer Science, University of KwaZulu-Natal, Westville Campus, Private Bag X54001, 4000 Durban, South Africa

[8] Atacama Large Millimeter/submillimeter Array, ALMA Santiago Central Offices, Alonso de Cordova 3107, Vitacura, Casilla 763 0355 Santiago, Chile

[9] CITA, University of Toronto, 60 St. George St., Toronto, ON M5S 3H8, Canada

[10] CNRS, IRAP, 9 Av. Colonel Roche, BP 44346, 31028 Toulouse Cedex 4, France

[11] California Institute of Technology, Pasadena, California, USA

[12] Centre for Theoretical Cosmology, DAMTP, University of Cambridge, Wilberforce Road, Cambridge CB3 0WA, UK

[13] Centro de Estudios de Física del Cosmos de Aragón (CEFCA), Plaza San Juan, 1, planta 2, 44001 Teruel, Spain

[14] Computational Cosmology Center, Lawrence Berkeley National Laboratory, Berkeley, California, USA

[15] DSM/Irfu/SPP, CEA-Saclay, 91191 Gif-sur-Yvette Cedex, France

[16] DTU Space, National Space Institute, Technical University of Denmark, Elektrovej 327, 2800 Kgs. Lyngby, Denmark

[17] Département de Physique Théorique, Université de Genève, 24 quai E. Ansermet, 1211 Genève 4, Switzerland

[18] Departamento de Física Fundamental, Facultad de Ciencias, Universidad de Salamanca, 37008 Salamanca, Spain

[19] Departamento de Física, Universidad de Oviedo, Avda. Calvo Sotelo s/n, 33007 Oviedo, Spain

[20] Department of Astronomy and Astrophysics, University of Toronto, 50 Saint George Street, Toronto, Ontario, Canada

[21] Department of Astrophysics/IMAPP, Radboud University Nijmegen, PO Box 9010, 6500 GL Nijmegen, The Netherlands

[22] Department of Electrical Engineering and Computer Sciences, University of California, Berkeley, California, USA

[23] Department of Physics & Astronomy, University of British Columbia, 6224 Agricultural Road, Vancouver, British Columbia, Canada

[24] Department of Physics and Astronomy, Dana and David Dornsife College of Letter, Arts and Sciences, University of Southern California, Los Angeles, CA 90089, USA

[25] Department of Physics and Astronomy, University College London, London WC1E 6BT, UK

[26] Department of Physics, Florida State University, Keen Physics Building, 77 Chieftan Way, Tallahassee, Florida, USA

[27] Department of Physics, Gustaf Hällströmin katu 2a, University of Helsinki, 00014 Helsinki, Finland

[28] Department of Physics, Princeton University, Princeton, New Jersey, USA

[29] Department of Physics, University of California, One Shields Avenue, Davis, California, USA

[30] Department of Physics, University of California, Santa Barbara, California, USA

[31] Department of Physics, University of Illinois at Urbana-Champaign, 1110 West Green Street, Urbana, Illinois, USA

[32] Dipartimento di Fisica e Astronomia G. Galilei, Università degli Studi di Padova, via Marzolo 8, 35131 Padova, Italy

[33] Dipartimento di Fisica e Scienze della Terra, Università di Ferrara, via Saragat 1, 44122 Ferrara, Italy

[34] Dipartimento di Fisica, Università La Sapienza, P.le A. Moro 2, 00185 Roma, Italy

[35] Dipartimento di Fisica, Università degli Studi di Milano, via Celoria, 16, 20133 Milano, Italy

[36] Dipartimento di Fisica, Università degli Studi di Trieste, via A. Valerio 2, 34127 Trieste, Italy

[37] Dipartimento di Fisica, Università di Roma Tor Vergata, via della Ricerca Scientifica 1, 00133 Roma, Italy

[38] Discovery Center, Niels Bohr Institute, Blegdamsvej 17, 2100 Copenhagen, Denmark

[39] European Southern Observatory, ESO Vitacura, Alonso de Cordova 3107, Vitacura, Casilla 19001 Santiago, Chile

[40] European Space Agency, ESAC, Planck Science Office, Camino bajo del Castillo, s/n, Urbanización Villafranca del Castillo, Villanueva de la Cañada, 28691 Madrid, Spain

[41] European Space Agency, ESTEC, Keplerlaan 1, 2201 AZ Noordwijk, The Netherlands

[42] Helsinki Institute of Physics, Gustaf Hällströmin katu 2, University of Helsinki, 00014 Helsinki, Finland

[43] INAF – Osservatorio Astrofisico di Catania, via S. Sofia 78, 95123 Catania, Italy

[44] INAF – Osservatorio Astronomico di Padova, Vicolo dell'Osservatorio 5, 35122 Padova, Italy

[45] INAF – Osservatorio Astronomico di Roma, via di Frascati 33, 00040 Monte Porzio Catone, Italy

[46] INAF – Osservatorio Astronomico di Trieste, via G.B. Tiepolo 11, 34131 Trieste, Italy

[47] INAF Istituto di Radioastronomia, via P. Gobetti 101, 40129 Bologna, Italy

[48] INAF/IASF Bologna, via Gobetti 101, 40129 Bologna, Italy

[49] INAF/IASF Milano, via E. Bassini 15, 20133 Milano, Italy

[50] INFN, Sezione di Bologna, via Irnerio 46, 40126 Bologna, Italy

[51] INFN, Sezione di Roma 1, Università di Roma Sapienza, Piazzale Aldo Moro 2, 00185 Roma, Italy

[52] IPAG: Institut de Planétologie et d'Astrophysique de Grenoble, Université Joseph Fourier, Grenoble 1/CNRS-INSU, UMR 5274, 38041 Grenoble, France

[53] IUCAA, Post Bag 4, Ganeshkhind, Pune University Campus, Pune 411 007, India

[54] Imperial College London, Astrophysics group, Blackett Laboratory, Prince Consort Road, London, SW7 2AZ, UK

[55] Infrared Processing and Analysis Center, California Institute of Technology, Pasadena, CA 91125, USA

[56] Institut Néel, CNRS, Université Joseph Fourier Grenoble I, 25 rue des Martyrs, 38042 Grenoble, France

[57] Institut Universitaire de France, 103, bd Saint-Michel, 75005 Paris, France

[58] Institut d'Astrophysique Spatiale, CNRS (UMR 8617) Université Paris-Sud 11, Bâtiment 121, 91405 Orsay, France

[59] Institut d'Astrophysique de Paris, CNRS (UMR 7095), 98bis boulevard Arago, 75014 Paris, France

[60] Institute for Space Sciences, 077125 Bucharest-Magurale, Romania

[61] Institute of Astronomy and Astrophysics, Academia Sinica, 10617 Taipei, Taiwan

[62] Institute of Astronomy, University of Cambridge, Madingley Road, Cambridge CB3 0HA, UK

[63] Institute of Theoretical Astrophysics, University of Oslo, Blindern, 0315 Oslo, Norway

[64] Instituto de Física de Cantabria (CSIC-Universidad de Cantabria), Avda. de los Castros s/n, 39005 Santander, Spain

[65] Jet Propulsion Laboratory, California Institute of Technology, 4800 Oak Grove Drive, Pasadena, California, USA

[66] Jodrell Bank Centre for Astrophysics, Alan Turing Building, School of Physics and Astronomy, The University of Manchester, Oxford Road, Manchester, M13 9PL, UK

[67] Kavli Institute for Cosmology Cambridge, Madingley Road, Cambridge, CB3 0HA, UK

[68] LAL, Université Paris-Sud, CNRS/IN2P3, Orsay, France

[69] LERMA, CNRS, Observatoire de Paris, 61 avenue de l'Observatoire, 75014 Paris, France

[70] Laboratoire AIM, IRFU/Service d'Astrophysique – CEA/DSM – CNRS – Université Paris Diderot, Bât. 709, CEA-Saclay, 91191 Gif-sur-Yvette Cedex, France

[71] Laboratoire Traitement et Communication de l'Information, CNRS (UMR 5141) and Télécom ParisTech, 46 rue Barrault, 75634 Paris Cedex 13, France

[72] Laboratoire de Physique Subatomique et de Cosmologie, Université Joseph Fourier Grenoble I, CNRS/IN2P3, Institut National Polytechnique de Grenoble, 53 rue des Martyrs, 38026 Grenoble Cedex, France

[73] Laboratoire de Physique Théorique, Université Paris-Sud 11 & CNRS, Bâtiment 210, 91405 Orsay, France

[74] Lawrence Berkeley National Laboratory, Berkeley, California, USA

[75] Max-Planck-Institut für Astrophysik, Karl-Schwarzschild-Str. 1, 85741 Garching, Germany

[76] McGill Physics, Ernest Rutherford Physics Building, McGill University, 3600 rue University, Montréal, QC, H3A 2T8, Canada

[77] National University of Ireland, Department of Experimental Physics, Maynooth, Co. Kildare, Ireland

[78] Niels Bohr Institute, Blegdamsvej 17, 2100 Copenhagen, Denmark

[79] Observational Cosmology, Mail Stop 367-17, California Institute of Technology, Pasadena, CA 91125, USA

[80] Optical Science Laboratory, University College London, Gower Street, London, UK

[81] SB-ITP-LPPC, EPFL, 1015, Lausanne, Switzerland

[82] SISSA, Astrophysics Sector, via Bonomea 265, 34136 Trieste, Italy

[83] School of Physics and Astronomy, Cardiff University, Queens Buildings, The Parade, Cardiff, CF24 3AA, UK

[84] Space Sciences Laboratory, University of California, Berkeley, California, USA

[85] Special Astrophysical Observatory, Russian Academy of Sciences, Nizhnij Arkhyz, Zelenchukskiy region, 369167 Karachai-Cherkessian Republic, Russia

[86] Stanford University, Dept of Physics, Varian Physics Bldg, 382 via Pueblo Mall, Stanford, California, USA

[87] Sub-Department of Astrophysics, University of Oxford, Keble Road, Oxford OX1 3RH, UK

[88] Theory Division, PH-TH, CERN, 1211 Geneva 23, Switzerland

[89] UPMC Univ Paris 06, UMR 7095, 98bis boulevard Arago, 75014, Paris, France

[90] Université de Toulouse, UPS-OMP, IRAP, 31028 Toulouse Cedex 4, France

[91] University of Granada, Departamento de Física Teórica y del Cosmos, Facultad de Ciencias, 1807 Granada, Spain

[92] Warsaw University Observatory, Aleje Ujazdowskie 4, 00-478 Warszawa, Poland